JOURNAL OF GEOPHYSICAL RESEARCH, VOL. 103, NO. B9, PAGES 21,165–21,182, SEPTEMBER 10, 1998

Topography on the 410-km seismic velocity discontinuity near subduction zones from stacking of *sS*, *sP*, and *pP* precursors

Megan P. Flanagan and Peter M. Shearer

Cecil H. and Ida M. Green Institute of Geophysics and Planetary Physics, Scripps Institution of Oceanography
University of California, San Diego, La Jolla

Abstract. We stack the teleseismic depth phases *sS*, *sP*, and *pP* produced by deep focus earthquakes to image precursory arrivals that result from near-source, underside reflections off the 410-km seismic velocity discontinuity (hereinafter referred to as the 410) and use differential time measurements between these phases and their precursors to compute discontinuity depths near seven subduction zones around the Pacific Ocean margin. We begin by selecting seismograms with high-quality depth phase arrivals recorded by several long-period networks between the years 1976 and 1996. Filtering the waveforms and stacking them along theoretical travel-time curves reveals clear precursors which vary in shape and timing. We compute confidence levels to evaluate the reliability of the observed precursory features using a bootstrap method that randomly resamples the seismograms prior to stacking. We measure the differential travel time between the reference pulse and the precursor using a cross-correlation technique and convert this time to an apparent discontinuity depth using the isotropic Preliminary Reference Earth Model (PREM) at 25-s period, corrected to an oceanic crustal thickness. The lateral resolution of our long-period stacks for 410 topography is limited compared to that sometimes achieved in short-period analyses but is much higher than that obtained from global *SS* precursor studies. For most subduction zones the results indicate little change in the average depth to the 410-km discontinuity in the local areas sampled by the precursor bounce points compared to broad regional depths inferred from *SS* precursor results. This implies that any large variations in depth to the 410-km discontinuity near subduction zones are limited to a narrow zone within the slab itself where they may be difficult to resolve with long-period data. Coverage for the Tonga and Peru-Chile subduction zones is sufficiently dense that we can observe lateral variations in 410 depths. In Tonga the results suggest depth variations perpendicular to the slab of up to 33 km, after correcting for probable lateral heterogeneity in velocity above 400 km depth, and variations parallel to the slab orientation as large as 13 km. The cross-slab variation is consistent with the elevation of olivine phase transformations in cold regions; the variation along strike suggests a more complex thermal heterogeneity that may be related to the subduction history of this region. We see evidence for additional reflectors above the 410 in some of the waveform stacks, but the inconsistency and weak amplitude of these features preclude definitive interpretations.

1. Introduction

Investigations of the sharpness, velocity contrast, and topography at the 410- and 660-km discontinuities bounding the mantle transition zone provide important constraints to plausible models of mantle composition, temperature, and convective processes. If these discontinuities are associated with polymorphic phase transitions in the olivine component of mantle material, their depths may vary as a result of lateral changes in mantle temperature [e.g., *Ringwood*, 1975]. Seismic constraints on the depths of the 410- and 660-km discontinuities (herein after referred to as the 410 and the 660) can be obtained through observations of secondary arrivals that result from reflections and phase conversions at these interfaces [e.g., *Vinnik*, 1977; *Revenaugh and Jordan*, 1989, 1991; *Shearer*, 1990, 1991]. Recently, long-period *SS* precursor observations have been used to produce global maps of discontinuity topography [*Shearer*, 1993; *Gossler and Kind*, 1996; *Gu and Dziewonski*, 1996; *Flanagan and Shearer*, 1998]. These maps show large-scale variations in depth to the 660 of about 35 to 40 km with somewhat lower amplitude topography (20 to 25 km) on the 410 that is largely uncorrelated with the 660 topography [*Flanagan and Shearer*, 1998]. Near subduction zones, where the largest lateral variations in temperatures might be expected, the 660 appears depressed by about 20 to 30 km, whereas no clear depth variations are apparent on the 410-km discontinuity.

The resolution of the *SS* precursor studies is limited, however, by the large Fresnel zones of the long-period *SS* waves; such studies are not expected to resolve small features comparable in scale to the width of subducting slabs. Much greater resolution can be achieved using near-source discontinuity phases from deep events within the subduction zones. A number of recent studies have measured mantle discontinuity depths near subduction zones using underside

Paper number 98JB00595.
0148-0227/98/98JB-00595$09.00

reflections and/or *S*-to-*P* converted phases [e.g., *Richards and Wicks*, 1990; *Bock and Kind*, 1991; *Vidale and Benz*, 1992; *Zhang and Lay*, 1993; *Yamazaki and Hirahara*, 1994; *Ritsema et al.*, 1995; *Castle and Creager*, 1997; *Collier and Helffrich*, 1997]. These studies generally indicate a slight elevation of the 410-km discontinuity and a depression in the 660-km discontinuity in the vicinity of subducting slabs, both of which are consistent with the expected thermodynamic response of the olivine phase changes at 410- and 660-km depth to the colder temperatures of subducted lithosphere.

In contrast, it is hypothesized that under certain temperature conditions a metastable form of olivine may persist in subducting slabs to depths well below 410-km depth and that the α–to β–olivine phase change provides a possible mechanism for the occurrence of deep earthquakes between 350 and 690 km [e.g., *Kirby*, 1987]. This hypothesis was supported by *Iidaka and Suetsugu* [1992], who concluded from a study of travel time residuals that metastable α–olivine exists to a depth of at least 550 km in the southwestern Japan subduction zone. Seismic evidence that deep focus earthquakes are related to the olivine-spinel transition also supports the existence of metastable olivine below the equilibrium phase boundary [*Helffrich and Brodholt*, 1991; *Wiens et al.*, 1993; *Iidaka and Furukawa*, 1994]. However, investigations by K. Koper et al. (Modeling the Tonga Slab: Can travel time data resolve a metastable olivine wedge?, submitted to *Journal of Geophysical Research*, 1998) indicate that seismic detection of a metastable olivine wedge may not be possible, and recent analyses [e.g., *Silver et al.*, 1995; *Myers et al.*, 1995] suggest that the 1994 deep Bolivian earthquake may not be compatible with the transformational faulting hypothesis.

The thermal structure of slabs depends primarily on the rate of subduction and on the age of the subducting lithosphere [e.g., *Molnar et al.*, 1979] and therefore varies greatly for different subduction zones. Experiments in which the thermal structure of subduction zones is modeled numerically [e.g., *Schubert et al.*, 1975; *Helffrich et al.*, 1989; *Helffrich and Brodholt*, 1991] indicate deformation of the 410 is predominantly controlled by temperature differences across the slab. Given that any elevation or depression of the transition zone phase boundaries will introduce buoyancy forces associated with density changes across the interfaces [e.g., *King and Hager*, 1994] (which will affect the rate at which the cold slabs sink into the mantle), mapping deflections of mantle discontinuities in the vicinity of subducting lithosphere can shed new light on kinetic and dynamic processes in Earth's mantle.

In this study, we measure topography on the 410-km discontinuity in several subduction zones by examining *sS*, *sP*, and *pP* precursors as observed from stacking long-period records from deep earthquakes. Rather than focusing on a single subduction zone or phase geometry, we adopt a comprehensive approach which incorporates all data currently available from the global digital archives in order to identify consistent features in the data and map lateral variations in the 410 wherever possible. In general, we find that the average depths to the 410-km discontinuity near subducting slabs are not significantly different from the broad regional averages obtained from *SS* precursor studies. A more detailed study of possible lateral variations in 410 depths is made for both the Tonga and Peru-Chile subduction zones; here we identify significant variations in the depth to the 410-km discontinuity but find that these variations are not related to the slab geometry in a simple manner.

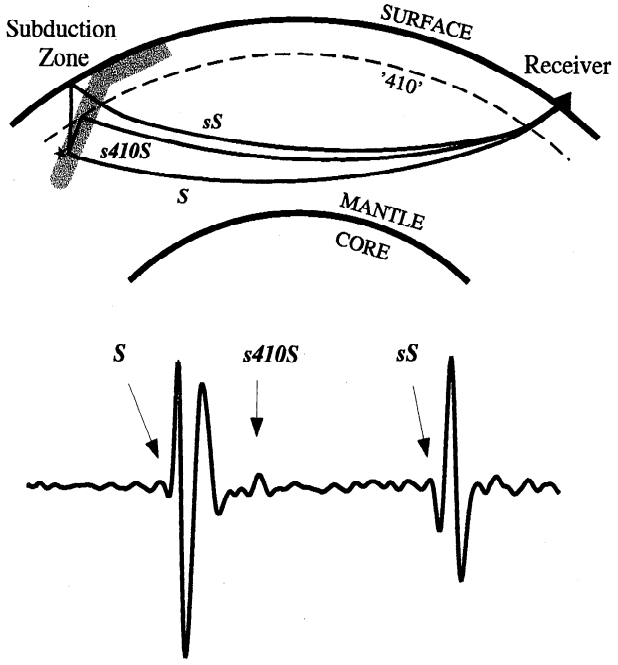

Figure 1. Earth cross-section displaying ray paths of *S*, *sS* and *s*410*S*; similar paths exist for *P*, *pP*, and *p*410*P* as well as the converted phases *sP* and *s*410*P*. The light gray region indicates subducting lithosphere, and the star represents a deep focus earthquake. The observed seismogram below shows the relative arrival of the direct, surface reflected, and 410 reflected phases respectively.

2. Precursors to *sS*, *sP*, and *pP*

Deep earthquakes will generate both upgoing and downgoing waves; as illustrated in Figure 1, the geometry of the upgoing phase *sS* illuminates the 410 boundary from below. The first arrival at a distant receiver will be the downgoing direct *S* wave, with the surface reflected *sS* phase arriving some time later. Our interest is in the secondary phase, *s*410*S*, which results from the underside reflection off the 410-km discontinuity and arrives in the time interval between *S* and *sS*. We generally do not observe *s*410*S* on individual seismograms because it is a weak arrival with an amplitude typically less than 5% of *sS*. However, we can make clearer observations of the *s*410*S* precursors by stacking and averaging many records together. The earthquake sources must have focal depths greater than 500 km to achieve a distinct separation between the direct *S* and *s*410*S* arrivals, restricting our approach to areas of very deep seismicity. Ray geometries for the *sP* and *pP* depth phases, together with the analogous discontinuity phases *s*410*P* and *p*410*P*, are similar to that shown in Figure 1 for *sS*. The underside reflection points on the 410-km discontinuity occur close to the source, and the depth phase precursors have much greater lateral resolution for discontinuity structure than can be obtained from *ScS* reverberation or *SS* precursor studies. Depending upon the source depth, receiver azimuth, phase type, and slab geometry, the underside bounce points on the 410 will generally lie near the region where the subducting slab intersects the discontinuity.

3. Data Selection

We conduct a survey of all subduction zones having substantial levels of deep seismicity (greater than 500 km

focal depth). The data are three-component digital long-period seismograms (1 Hz sample rate) recorded by the Global Digital Seismograph Network (GDSN), Incorporated Research Institutions for Seismology-International Deployment of Accelerometers (IRIS-IDA), and Geoscope networks and are divided into two parts. The long-period Seismic Research Observatory (SRO) data set (LP_{SRO}) comprises recordings between 1976 and 1997 with the data recorded after 1988 low-pass filtered (using the SRO instrument response for station Albuquerque, New Mexico (ANMO)) to match the frequency content of the older data; the resultant waveforms have dominant energy at 0.04 Hz. The long-period (LP) data set contains records between the years 1988 and 1997 exclusively. These data are recorded at stations with instruments having a broad response function that permits us to filter over a number of frequency bands between 0.01 and 1.0 Hz (these filters are described in more detail below). In a few cases, particular stations did not have the appropriate instrument response to allow filtering (e.g., some from the Chinese Digital Seismic Network and Geoscope stations) and were thus excluded.

We compile both vertical- and transverse-component seismograms for all earthquakes of focal depth > 500 km, in the epicentral distance range 75° to 125°, and having body wave magnitude m_b > 5.5 for a total of 14,671 records; epicentral information is taken from the monthly Preliminary Determination of Earthquakes (PDE) bulletins of the U.S. Geological Survey. Next, we apply an automated procedure to select those records containing a depth phase (*sS*, *sP*, or *pP*) with a local signal-to-noise (STN) ratio of 3 or greater. We estimate the STN by dividing the maximum amplitude of the reference phase by the maximum amplitude in a "noise" window immediately preceding the reference arrival. Finally, we visually examine each of these records, hand-pick the maximum peak of the depth phase, and assign a grade (A, B, or C) based on the STN ratio and the clarity of the reference waveform. Manually editing the data assures the inclusion of those records with clean reference pulse shapes, free of erroneous arrivals immediately before or after the pulse, and the exclusion of traces with aftershock arrivals in the time window of interest. This process reduces the number of data to approximately 1562 transverse-component and 1540 vertical-component, LP_{SRO} seismograms and 1155 transverse-component and 1083 vertical-component, LP seismograms.

The data coverage in seven subduction zones is shown in Figure 2; the solid triangles represent the bounce point locations of the *sS*, *pP*, and *sP* phases used in this study. The largest portion of the data comes from Tonga (*sS*=538, *sP*=583, *pP*=417 records) and South America (*sS*=242, *sP*=243, *pP*=112 records); other subduction zones include Java (*sS*=50, *sP*=163, *pP*=19 records), Philippines (*sS*=23, *sP*=17, *pP*=2 records), Marianas (*sS*=40, *sP*=70, *pP*=27 records), Japan (*sS*=23, *sP*=13, *pP*=17 records), and Kuril (*sS*=25, *sP*=16, *pP*=9 records). The numbers listed here for *sS* and *sP* are for the LP_{SRO} data set. For the *pP* data we were restricted to using only the LP records because the LP_{SRO} records did not show a clear time separation of the *p*410*P* precursor from the main *P* phase (except for very deep events > 600 km focal depth). Consequently, there are fewer events for which we have suitable *pP* data, and the *pP* stacks contain fewer traces.

Examples of transverse- and vertical-component seismograms are shown in Figure 3 with the arrival times of the relevant phases computed using the iasp91 velocity model [*Kennett*, 1991]. In these examples we find small pulses near

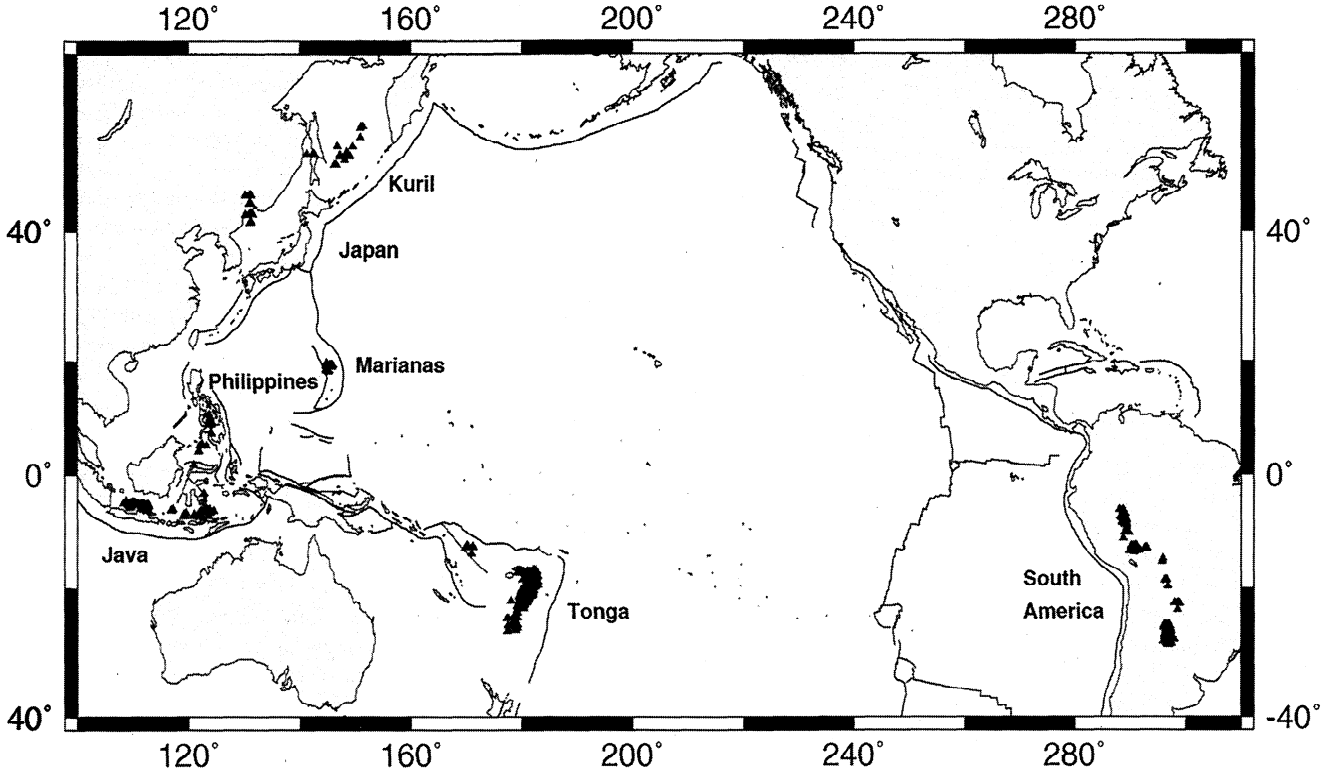

Figure 2. Bounce point locations (triangles) of *sS*, *pP*, and *sP* phases from the 822 deep focus earthquakes (>500 km) examined in this study. Of the seven subduction zones considered here, Tonga and South America have the most extensive data coverage, allowing us to investigate lateral variations in discontinuity structure for these two regions.

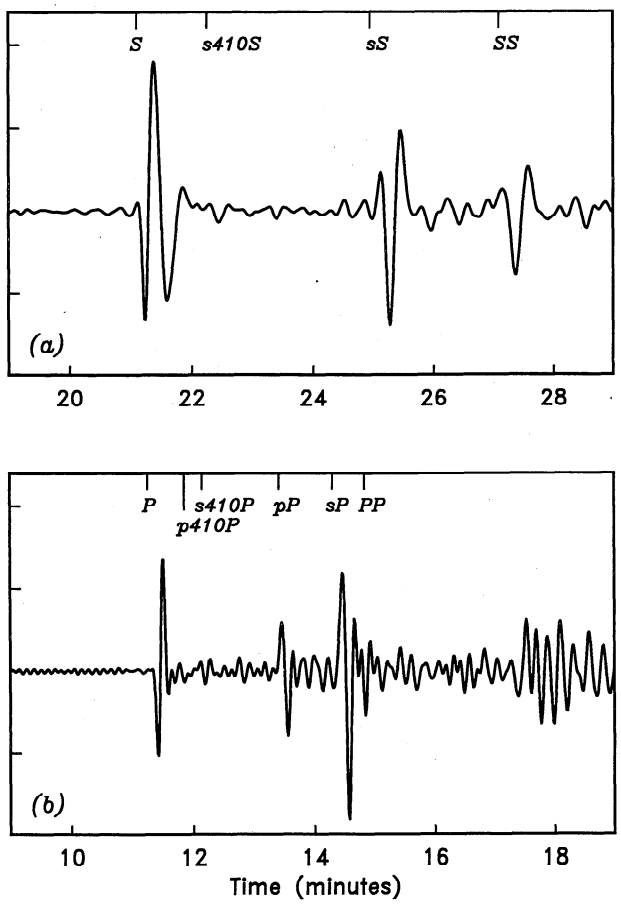

Figure 3. (a) LP_{SRO} transverse component seismogram from a 605-km-deep event in the Kuril recorded at station HRV at 84° range. (**b**) LP vertical component seismogram from a 566-km-deep event in Tonga recorded at station COR at 83° range. The horizontal axis is minutes after origin time as computed from the iasp91 velocity model with the phases marked above the corresponding arrivals. Note the energy arriving at times corresponding to the precursors *s*410*S* and *s*410*P*, although the identification of the *p*410*P* phase is sometimes ambiguous due to its proximity to *s*410*P* (arriving within 20 s).

the expected arrival times for the underside reflections *s*410*S* and *s*410*P*. However, we rarely observe the discontinuity phases with such clarity on individual seismograms; in general, large numbers of records must be combined together to obtain robust observations. We accomplish this through a stacking procedure that reduces the incoherent noise levels while enhancing the coherent arrivals associated with the discontinuity reflections. Stacking also helps us to distinguish between the *s*410*P* and *p*410*P* phases which are often closely spaced on the individual seismograms (see Figure 3b). There are several mantle *P* waves and *P*-to-*S* conversions between the main *P* arrival and the *sP* phase, but because the polarities of *sP* and *pP* often vary (due to source radiation patterns), stacking each of these phases separately tends to enhance the visibility of the targeted phase and its precursor at the expense of the other depth phase.

4. Waveform Stacking Procedure

To investigate variations of the depth to the 410, we employ a waveform stacking procedure adapted from *Shearer* [1996]. We process the transverse- and vertical-component records separately and stack them with a weighting that gives preference to those traces with the highest STN ratios. For transverse components the stacking procedure is illustrated in Figure 4a, a time versus range plot of LP_{SRO} records from different earthquakes, showing *sS* and its precursors. Similarly, Figure 4b shows LP vertical component records with *sP*, *pP*, and their precursors. The arrivals are identified at the top and the theoretical arrival times based on the iasp91 velocity model [*Kennett*, 1991] are shown by solid lines (for the primary phases) and dashed lines (for the discontinuity phase). We align the traces on *sS* or *sP*, then stack along the theoretical move-out curve for the *s*410*S* or *s*410*P* precursor, essentially collapsing all traces into a single reflectivity profile, shown as the composite stack at the bottom of Figures 4aand 4b. Although not illustrated explicitly, the same procedure is performed for the *pP* phase seen in Figure 4b. We restrict epicentral distances to 80° to 125° for the *sS* stack to avoid interference from the *ScS* phase and 75° to 125° for the *sP* and *pP* phases to avoid interference from the *PcP* phase on the vertical-component records. Note that *S* is generally phase-reversed relative to *sS*, a result of the source radiation pattern, but *s*410*S* has the same polarity as *sS*. In Figure 4b the polarity of the *sP* and *pP* phases are not always the same, a factor that is helpful in identifying their 410 precursors (which will mimic the depth phases *sP* and *pP* as they do for *sS*). The polarity of the reference pulse (*sS*, *sP*, or *pP*) is always preserved such that the energy of the associated precursor stacks coherently.

The result of stacking the tangential (for *sS*) and vertical (for *sP* and *pP*) records from all of the subduction zones on the *s*410*S*, *s*410*P*, and *p*410*P* precursors is seen in Figure 5. The traces to the left of the dashed vertical lines have been stacked along the predicted travel time curves for *s*410*S*, *s*410*P*, and *p*410*P*, respectively, assuming a reference range of 90°. The amplitude of this portion of the stack is magnified by a factor of 10 to enhance the visibility of the precursors. To the right of the dashed lines the reference phase is stacked along the predicted travel time curve for the appropriate depth phase, then aligned at zero time and normalized to unit amplitude. The strong peaks at 2 to 4 min before the depth phases are the direct *S* and *P* arrivals, which appear distorted since the scatter in focal depth causes them to stack incoherently. The thick trace represents the actual stack of the data, while the thin lines represent 95% confidence levels computed using a bootstrap method in which we repeat the stack many times for random samples of the data. These bounds provide a measure of the statistical reliability of features in the stack. Note that the stacking procedure on the vertical-component records succeeds in separately emphasizing the *sP* and *pP* depth phases with only a small contribution from the other depth phase remaining visible on each stack (see Figures 5b and 5c, respectively). This suggests that contamination from *p*410*P* on the *s*410*P* stack (and vice versa) will be minimal.

The small peaks that follow direct *S* and *P* in these data stacks are the underside reflections from the 410-km discontinuity. We measure the differential time between these arrivals and the reference wavelet by cross-correlating the two waveforms, then convert the measured time difference to a depth estimate for the 410 reflector by assuming a reference velocity model. We use isotropic Preliminary Reference Earth Model (PREM) [*Dziewonski and Anderson*, 1981] at 25 s corrected for an oceanic bathymetry and crustal thickness (as the bulk of the data have surface bounce points in oceanic

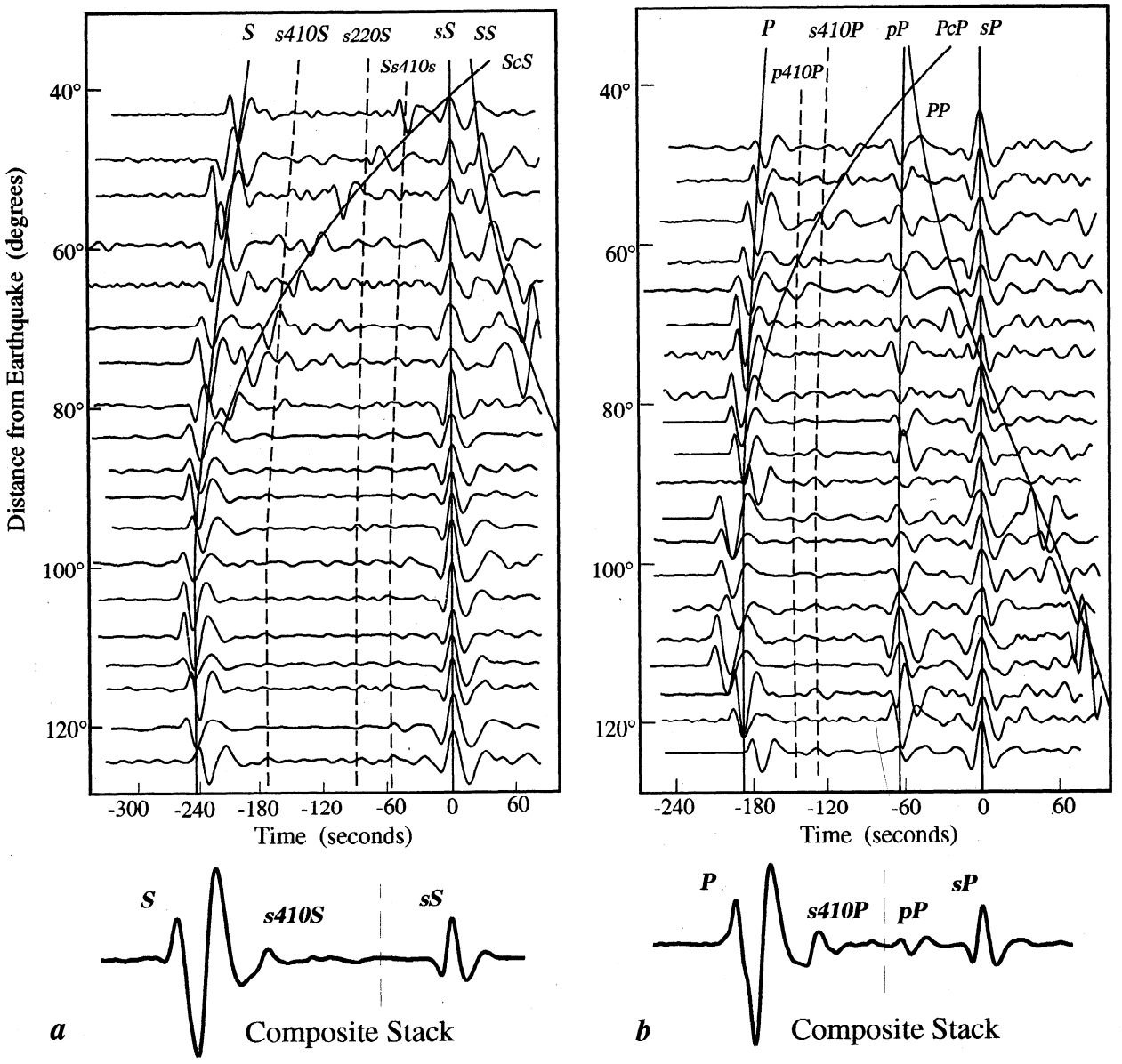

Figure 4. (a) Time versus range plot showing the reference pulse *sS* and its precursors. The waveforms shown are a small subset of the data chosen to illustrate the stacking procedure. Travel time curves computed from iasp91 (for a 600 km source depth) are overlain and show the predicted arrival time of each phase. Traces are aligned on the reference pulse *sS* and stacked along the moveout curve for the *s*410*S* phase to image the precursors (left of dashed line) while the reference pulse is stacked separately on the *sS* moveout curve (right of dashed line). The composite stack shown at bottom, at a reference range of 90°, comprises only records from 80° to 125° to avoid contributions from *ScS*. (b) Analogous time versus range plot of vertical component seismograms aligned on the *sP* reference pulse together with the travel time curves for the primary phases (solid lines) and discontinuity phases (dashed lines) of both *sP* and *pP*. Stacks for the *s*410*P* and *p*410*P* precursors are made by aligning on the *sP* or *pP* phase, respectively, and the composite stack at bottom comprises only records between 75° and 125° to avoid interference from *PcP*.

backarc regions); only for the South American subduction zone did we use the standard isotropic PREM with the original 24.4 km crust which is more representative of this region. The choice of velocity model directly affects the depth estimates for the 410 and is discussed further below. The cross correlation is accurate to 1 s, as the sampling rate of the data is 1 Hz; however, a better estimate of the standard error in these measurements can be made from the bootstrap procedure. We obtain a differential time separately from each of the random stacks and use the distribution of these measurements to compute the standard error of the differential time. We then use the reference velocity model to convert the measured timing errors into estimates of the uncertainties in the discontinuity depths.

The errors in the measured differential times largely result from the coherence of the stacking, which is a function of the number and quality of the seismograms composing the stack. Mislocation of the earthquake sources themselves does not contribute significant error because we are concerned only with the differential time between the surface reflection and the precursor, which is nearly independent of the time between the main phase and the depth phase. However, velocity variations

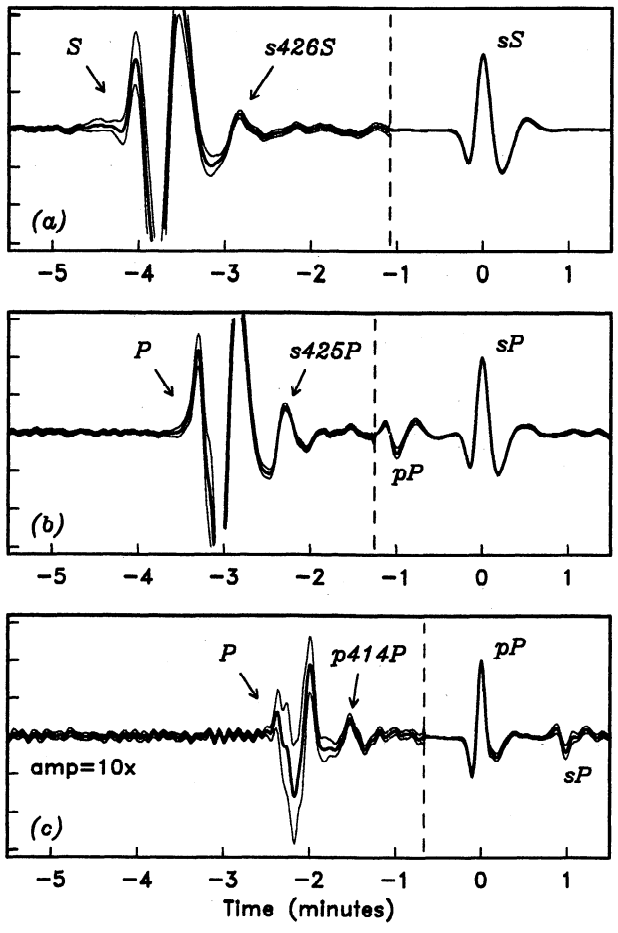

Figure 5. Stacks of the data from all regions for (a) *sS*, (b) *sP*, and (c) *pP*. The thick trace represents the actual stack of the data, and the thin lines show the 95% confidence levels. The horizontal axes are time in minutes with respect to the stacking phase; the reference pulse is normalized to unit amplitude after stacking. The trace to the left of the dashed line is magnified by a factor of 10 for display purposes. Significant levels of energy arriving between the direct phase and the surface-reflected phase indicate the presence of velocity discontinuities in the shallow mantle. The depth indicated in each panel has been computed from the differential travel time between the surface reflection and its precursor; the depths indicated have standard errors of 1 to 2 km.

along the raypath of the depth phases can be significant in subduction zones which are often characterized by fast slabs and slow backarcs [e.g., *van der Hilst et al.*, 1991]. These variations may affect the conversion of the times to depths and are addressed below.

Globally averaged depth estimates to the 410-km discontinuity for the three different stacks are indicated on Figure 5: 426 km for the *sS* precursors, 425 km for the *sP* precursors, and 414 km for the *pP* precursors. The *sS* precursor depths are somewhat greater than globally averaged depths as measured from *SS* precursors (e.g., 418 km from *Flanagan and Shearer* [1998]), but this overall offset in the depths should not be considered significant as the difference arises from details in the topography and crustal thickness corrections. Later, we compare our *sS* 410 depth estimates more directly with *SS* precursor results by stacking *SS* data using the same stacking method and reference velocity model that is used in this study of the depth phases.

The average depth estimates from the *sS* and *sP* precursors are in excellent agreement, but the *pP* results give a 410 depth estimate that is significantly shallower. As will be shown in sections 6 and 7, this difference appears consistently in our analyses even when the data are subdivided into different geographical regions. We have considered several possible origins for this discrepancy. If the *pP* surface bounce points actually occur at the top of the ocean, rather than the bottom as we assume, this would bias the *pP* 410 estimates to greater, not shallower, depths. Conceivably, discontinuity phases associated with *sP* might introduce some bias in the *pP* stacks, but the amplitude of *sP* is only 20% that of *pP* (on the *pP* stack) implying that such contamination should be minor. The most likely explanation for the observed difference between the *s*410*S* and *p*410*P* inferred depths is that the average *P*-to-*S* velocity ratio in the upper mantle is slightly larger than the value given in the isotropic version of PREM. A 3% increase in the *Vp*/*Vs* ratio (assuming a 1.5% change in each) would produce revised depth estimates of 420 km for the *sS* precursors, 423 km for the *sP* precursors and 420 km for the *pP* precursors. This slightly worsens the agreement between the *sS* and *sP* precursors, but the overall consistency between the three phase types is improved. An increase in the *Vp*/*Vs* ratio from PREM could result from anomalously low *S* velocities in the backarc regions of the subduction zones [e.g., *Xu and Wiens*, 1997]. Thus we believe that the depth discrepancy is best explained as a result of the fact that the Vp/*Vs* ratio in the PREM velocity model we use to compute the depths is not representative of the velocities which exist in the subduction zones our data sample. However, we choose not to apply a correction to bring the depths into better agreement, as such a correction would be ad hoc and would prevent direct comparison of the *sS* precursor results with the global *SS* precursor study of *Flanagan and Shearer* [1998]. Ideally, one could compute 410 depths from our measured times using regional velocity models for each individual subduction zone (for this purpose, all measured differential times for each waveform stack in each region are available from the authors via e-mail or anonymous ftp at mahi.ucsd.edu in the /pub/THE410 directory).

Since the 410 precursors closely follow the direct *S* and *P* arrivals, sidelobe interference from the direct phases could bias our observations. To explore this further, we perform a number of tests to assess reliability of the 410 peaks, experimenting with the filtering parameters and focal depth criteria. The separation in time of the *s*410*S* and *p*410*P* precursors from the *S* and *P* arrivals, respectively, is a function of both the depth of the earthquake and the frequency content of the data (and to a lesser degree epicentral range). We experiment with a variety of filters and focal depth bins to find the appropriate cutoff values which allow us to image the precursors accurately for each type of stack (i.e., *sS* , *sP*, *pP*).

The LP_{SRO} *sS* stacks in Figure 6 are made using different cutoff values for the minimum focal depth. Note that the 410 peak becomes increasingly distinct from direct *S* as we progressively restrict the focal depth range of considered events. However, the depth estimates derived from the 410 arrival times do not show a large variation, with the lower three plots agreeing within 2 km. After several tests with each depth phase, we choose 550 km as the focal depth cutoff value

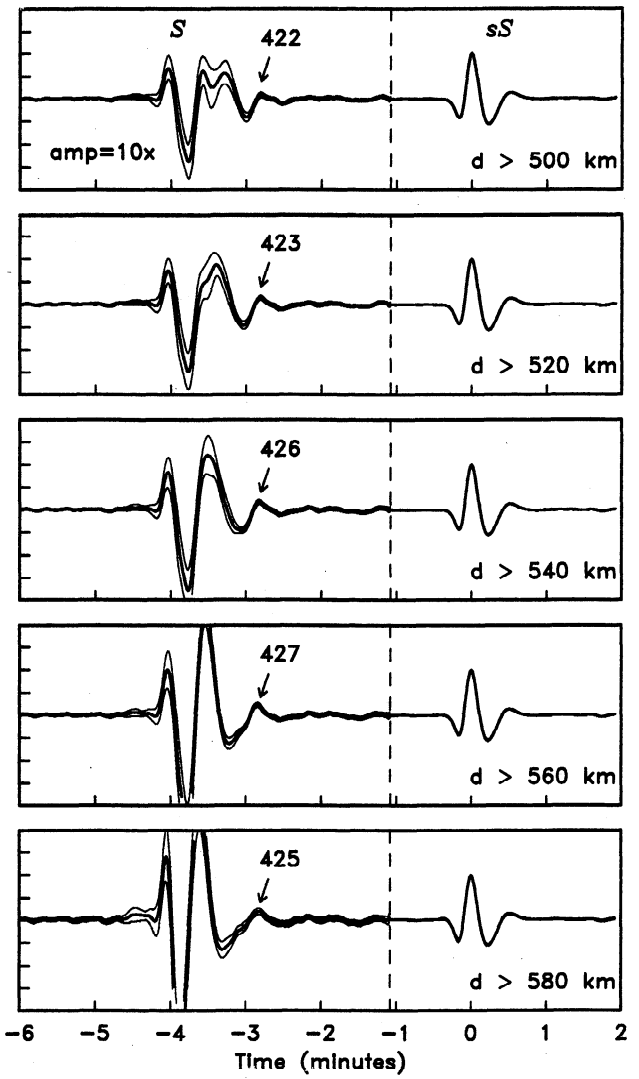

Figure 6. LP_{SRO} *sS* stacks made using sets of seismograms with different upper limits on focal depths (*d*) showing that the *s*410*S* precursor pulse is not a sidelobe of the direct *S* pulse. Note as we eliminate the shallower earthquakes above 540 km depth, the precursor becomes well separated from the main pulse and less muted in amplitude and gives consistent depth estimates to the 410. This demonstrates the reliability of the stacking method to effectively isolate underside reflections from the 410-km discontinuity.

for both the *sS* and *sP* LP_{SRO} stacks and 530 km for the *pP* LP stack.

In Figure 7 we show the result of applying different filters to the LP *sP* records prior to stacking. The precursor pulse changes in shape and amplitude as higher frequencies are included, but its arrival time remains the same. The use of higher-frequency data aids greatly in resolving the separation of the 410 precursor from the main phase. This consistency is vital to precisely measuring the timing as we desire a standard measurement technique to apply to a variety of stacks. Note also that as we include higher frequencies, other features appear, possibly indicating other discontinuities above 410 km (e.g., the small pulse about 110 s before *sP* in Figure 7, bottom panel) . For the LP stacks we can include waveforms from shallower events, as the frequency content allows for better separation of the precursor from the main phase. For the remaining stacks we choose the filters and focal depth limits which allow inclusion of the greatest number of seismograms in the stacks, as some regions are very sparsely sampled.

The *S* waves (seen on the transverse component) typically have cleaner records and simpler pulse shapes than the *P* waves (seen on the vertical component), which typically have higher frequency content but are more noisy and cluttered with converted phases. Stacking the *pP* phase requires LP data exclusively because the time separation is not as great as for *sS* and *sP; p*410*P* arrives too close in time after the main *P* phase to be reliably identified on LP_{SRO} records. We use both sets of records to examine the *sS* and *sP* phases, as the *s*410*S* and *s*410*P* precursors are well separated from the main *S* and *P* pulses. We also observe evidence for additional reflectors above the 410 in some of the stacks, but the inconsistency

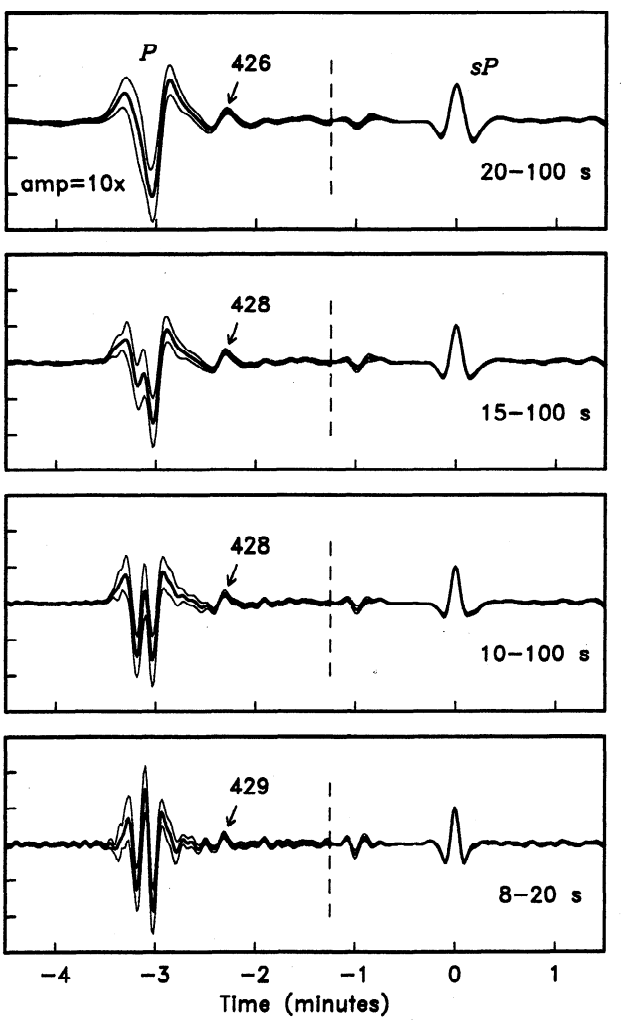

Figure 7. LP *sP* stacks using filters and showing the clarity of the low amplitude *s*410*P* arrivals, and coherence over different frequency bands as labeled. The top stack with a filter between 20 and 100 s period is similar to the LP_{SRO} *sP* stack shown in Figure 5b. Note how the precursor becomes sharper and more distinct from the main *P* phase as shorter-period energy is included in the stack.

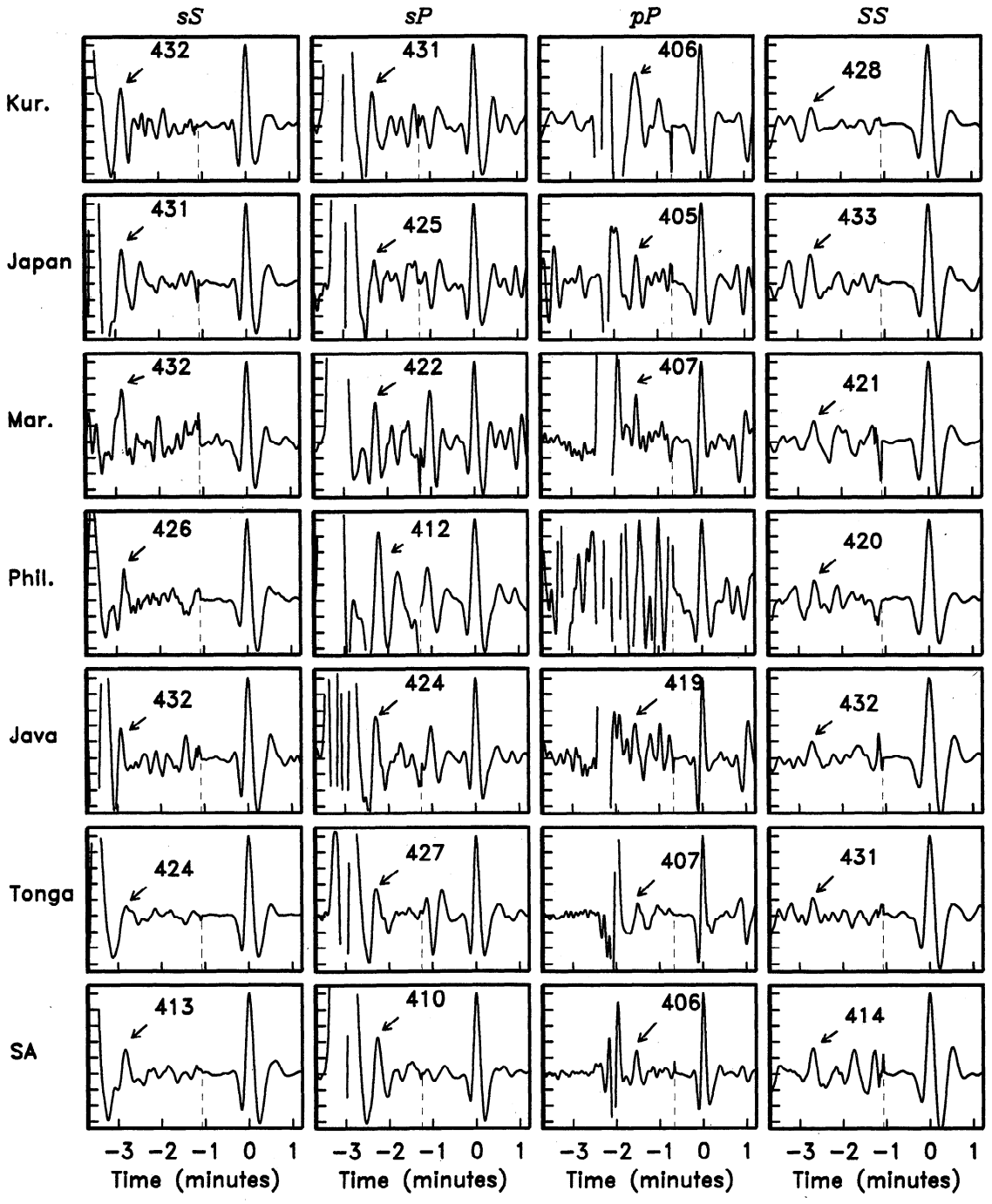

Figure 8. Regional *sS*, *sP*, *pP*, and *SS* stacks for seven subduction zones as indicated in the title of each panel. These stacks are made from all LP_{SRO} records available except for *pP* in which case only the LP data are used. The trace to the left of the dashed line is magnified by a factor of 10 for display purposes. Where a clear 410 precursor peak is imaged, the corresponding depth is labeled with an arrow and is listed in Table 1 along with its standard error. The *sS* and *sP* results roughly agree for most regions; the *pP* results, however, indicate systematically shallower depths (see text).

and weak amplitude of these features preclude definitive interpretation at this time. For example, the hint of a peak about 130 s before *sS* in Figure 6 coincides with the predicted position of a near-source reflection at about 300 km depth (*s*300*S*). Similarly, the peak arriving 110 s before *sP* in Figure 7 corresponds to a near-source reflector at a depth of either 350 km (*s*350*P*) or 220 km (*p*220*P*).

5. Individual Subduction Zones

Next, we present results for the different subduction zones shown in Figure 2; the individual *sS*, *sP* and *pP* stacks are plotted in Figure 8. Not all stacks produce clear 410 precursor peaks, but we show the results in their entirety to demonstrate the variability in the data and the range of reliable features in

Table 1. Raw 410 Depth Estimates for All Subduction Zones

Region	*sS*			*sP*			*pP*			*SS*		
	Number of Data	Depth, km	±σ, km	Number of Data	Depth, km	±σ, km	Number of Data	Depth, km	±σ, km	Number of Data	Depth, km	±σ,* km
Kuril	25	432	1	16	431	2	9	406	3	394	428	3
Japan	23	431	1	13	425	3	17	405	5	110	433	3
Marianas	40	432	3	70	422	3	27	407	2	41	421	5
Phil.	23	426	2	17	412	4	2	-	-	73	420	3
Java	50	432	3	163	424	5	19	419	6	77	432	4
Tonga	538	424	2	583	427	2	417	407	2	76	431	4
So. Am.	242	413	2	243	410	2	112	406	3	96	414	3

* Uncertainties are one standard deviation computed from bootstrap algorithm.

the stacks. In almost every region, clear precursor peaks can be identified, and the 410 depth estimates are labeled; these depths along with their standard errors are listed in Table 1. Also, to make specific comparisons with regional estimates of 410 depths determined from long-period *SS* precursor observations (see *Flanagan and Shearer* [1998]), for more details about the *SS* precursor data set), we stack *SS* data within bounce point caps 20° across, centered on each of the subduction zones for which we have depth phase data. Results of these stacks are shown in the rightmost column of Figure 8, and the depth estimates obtained from the *SS* precursor peaks (*S410S* arrivals) are labeled. For consistency with the depth phase results the *SS* precursor depths are determined using the same oceanic PREM [*Dziewonski and Anderson*, 1981].

The average absolute discontinuity depths depend upon the specific velocity and crustal models used to correct the times to depths; this accounts for the differences between the *SS* precursor results shown here and the 410-km discontinuity topography maps presented by *Flanagan and Shearer* [1998]. Note that the *pP* precursor depth estimates are generally significantly less than the *sS* and *sP* estimates; as discussed in section 4, this probably results from inaccuracies in the *Vp/Vs* ratio in the assumed velocity model. We do not attempt in this study to correct the 410 depths for large-scale three-dimensional velocity structure in the upper mantle. Rather our interest is in possible small-scale topography on the 410-km discontinuity, which can be detected in two different ways.

First, a difference might be seen between the local depth estimates derived from the depth phase precursors and the broader regional averages obtained from the *SS* precursors. The Fresnel zone for the long-period *S410S* reflections is about 15° across, while the Fresnel zones for the depth phase bounce points on the 410 are generally 2° across. Thus a difference between the 410 depths obtained from the depth phase precursors and those obtained in the same area from the *SS* precursors could indicate a difference between the local near-slab 410 depths and the average depth in the surrounding region. The advantage of this approach is that large-scale variations in crustal structure and velocity heterogeneity in the upper mantle will bias both data sets in the same way (although local velocity heterogeneity may be problematic, as discussed in section 8). Second, in regions with sufficient data it may be possible to directly resolve local variations in 410 topography by stacking subsets of the data grouped by their bounce point location. In sections 6 and 7 we apply this approach to the South American and Tonga data.

The most reliable local estimate for the 410 depth in the Kuril subduction zone (see Figure 8) is 432-431 km, provided by the *sP* and *sS* stacks (the *pP* results give a much shallower estimate of 406 km but with a larger standard error); this is reasonably close to the *SS* precursor depth estimate of 428 km. For the Japan subduction zone the clearest 410 peak in the depth phase precursors is for *sS*, which yields a depth estimate of 431 km, very close to the value of 433 km

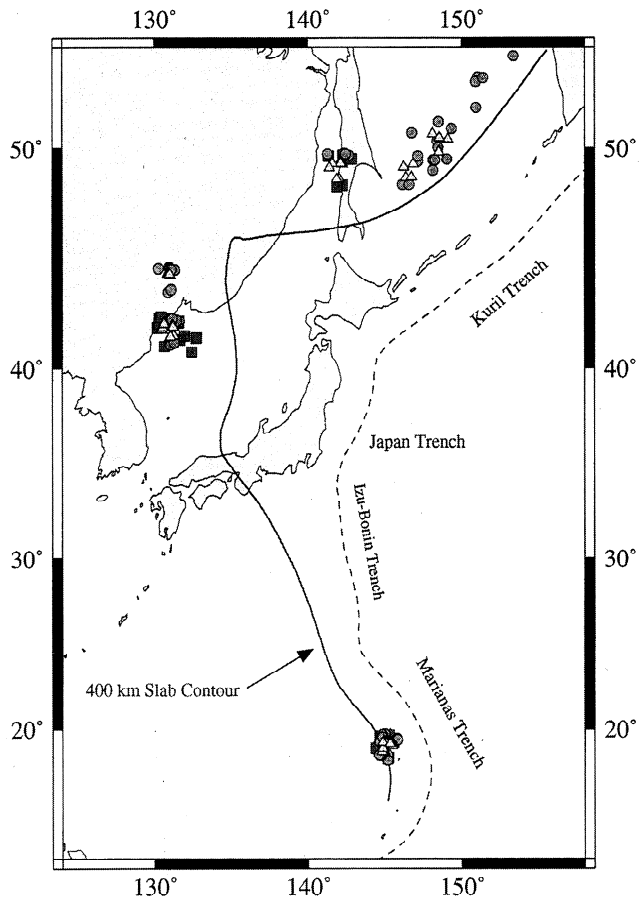

Figure 9. Mercator projection of the northwest Pacific Ocean margin showing the Kuril, Japan, and Marianas subduction zones together with the bounce point locations of *s410S* (circles), *s410P* (triangles), and *p410P* (squares) as they sample 400 km depth. Contours of the subducted lithosphere are shown at the surface trench location (dashed line) and 400 km depth (solid line). For Kuril and Japan the bounce points are far from the slab, whereas in Marianas they cluster close to the slab. The slab contours are taken from *Gudmundsson and Sambridge* [1998].

obtained from the *SS* precursors. Thus a significant change in 410 depths near the subducting slab is not indicated from our Kuril and Japan stacks. We estimate that the data in these stacks sample the 410-km discontinuity 100 to 300 km away (to the west) from where the subducting slab actually intersects the discontinuity, as seen in Figure 9. The maps in Figures 9-11 coincide with the waveform stacks of Figure 8 and illustrate the positions of our 410 bounce points (*sS* circles, *pP* squares, *sP* triangles) relative to the 400-km depth contour for the slab as determined by *Gudmundsson and Sambridge* [1998]. These contours are produced by fitting surfaces to patterns of seismicity at 50 km depth intervals and represent the top of the seismogenic region.

The Marianas 410 bounce points appear to sample within or very close to the subducting slab (Figure 9), providing our best test, aside from Tonga, of the direct response of the 410-km discontinuity to the cold slab. The Marianas *sP* and *SS* stacks produce similar depth estimates of 422 and 421 km, respectively (Figure 8). The *sS* estimate is somewhat deeper at 432 km, providing limited evidence to support a depression in the 410 within the slab, while the *pP* estimate is again shallower at 407 km. The origin of the difference between the *sS* and *sP* results is not obvious as both have fairly small standard errors: 3 km each. The *sS* and *sP* bounce point locations are almost identical; however, the Fresnel zone for *sP* is significantly smaller than that for *sS*, so differences in resolution may account for some of the discrepancy if

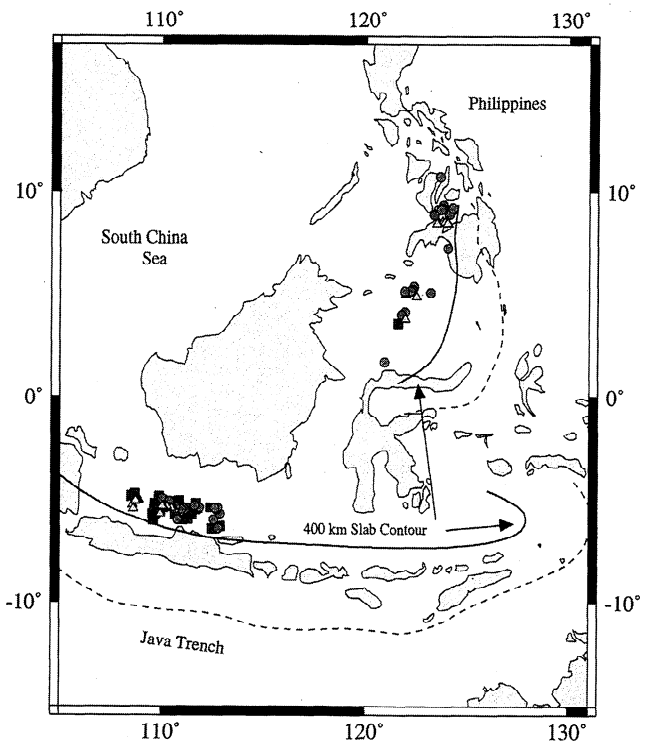

Figure 10. Mercator projection of the Java and Philippines subduction zones together with the bounce point locations of *s*410*S* (circles), *s*410*P* (triangles), and *p*410*P* (squares) as they sample 400 km depth. As in Figure 9, contours of the subducted lithosphere are shown at the surface trench (dashed line) and 400 km depth (solid line). For the Philippines the bounce points are far from the slab, whereas in Java, some samples are close to the slab. The slab contours are taken from *Gudmundsson and Sambridge* [1998].

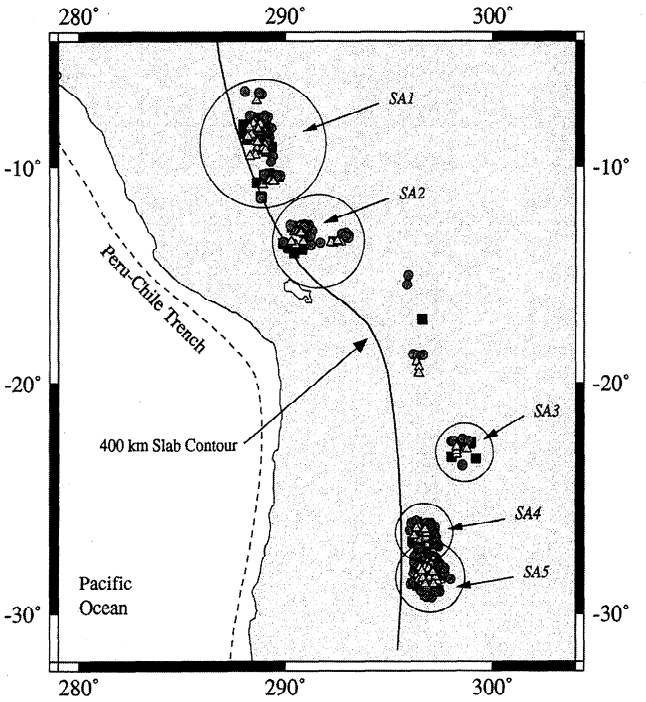

Figure 11. Mercator projection of South America showing the Peru and Chile subduction zones together with the bounce point locations of *s*410*S* (circles), *s*410*P* (triangles), and *p*410*P* (squares) as they sample 400 km depth. As in Figure 9, contours of the subducted lithosphere are shown at the surface trench (dashed line) and 400 km depth (solid line). The bounce points in clusters SA1 and SA2 are closest to the slab, clusters SA4 and SA5 are slightly farther away, and cluster SA3 is farthest from the slab. The slab contours are taken from *Gudmundsson and Sambridge* [1998].

significant short-wavelength lateral variations in 410 topography are present.

In the Philippines the bounce points are 100 to 200 km west of the slab intersection line (Figure 10). The *sS* and *SS* depth estimates are fairly close (426 and 420 km); the *sP* stack indicates a shallower depth of 412 km but is derived from only 17 seismograms. A stack of *pP* data could not be obtained because there were only two records. For Java the bounce points lie about 100 km north of the slab and the estimates from *sS*, *sP*, and *SS* are all in good agreement (432, 424 and 432 km), while the *pP* stack gives a depth of 419 km but with a large standard error of 6 km. For both the Philippines and Java, it appears that the 410-km discontinuity does not vary by more than 5 to 8 km from the average depth in the surrounding region as measured by the *SS* precursor data (Figure 8).

For the Tonga subduction zone the *sS*, *sP*, and *SS* stacks yield depth estimates of 424, 427, and 431 km; the *pP* stack indicates a significantly shallower 410-km discontinuity than the *sS* and *sP* stacks (see discussion in section 4). Note the low amplitude of the 410 precursor peak in both the *sS* and *pP* stacks for Tonga, an unexpected observation considering the very high number of data comprising them. We will explore this feature of the Tonga data in more detail in section 7.

In South America, the bounce point distribution spans both the northern and southern parts of the Peru-Chile Trench as illustrated in Figure 11. We begin by combining all the data

together to produce the stacks shown at the bottom of Figure 8. For the South American data we use the standard PREM (with the oceans filled in) to compute discontinuity depths, rather than the oceanic PREM used for the other regions. This results in 410 depths which are 10-15 km more shallow than those computed with the oceanic velocity model. The *sS* and *sP* stacks yield 410 estimates of 413 and 410 km which are in good agreement with the regional estimate of 414 from the *SS* stack; the *pP* stack indicates a slightly shallower depth of 406 km. Next, we experiment with stacking subsets of these data grouped by their bounce point locations since the data sample a larger geographic region than any other subduction zone.

6. South American Subduction Zone

We examine five distinct subclusters of the South American data, shown by the circles in Figure 11 with the accompanying waveform stacks in Figure 12 and Table 2; the bounce point clusters at the intermediate latitudes did not produce coherent stacks as the data are too few. Each group of bounce points is located about 100 km east of the slab, except for cluster SA3 which lies about 300 km from the slab. For the northernmost cluster SA1 the *sP* and *pP* stacks agree well with estimates of 398 km; the *sS* stack produces an estimate of 404 km but the 410 precursor in this stack is questionable despite its very small error estimate. (Depths for this region only are computed using the standard PREM, as noted above.) Cluster SA2 just to the south shows only one reliable estimate, 404 km, from the *sP* stack. Moving farther south, cluster SA3 shows a consistently deeper discontinuity depth of 416 to 430 km from all three *sP*, *sS*, and *pP* stacks. Although this is in better agreement with the regional estimate of 414 km from the *SS* stack in Figure 8, the low number of records and the high standard errors for these stacks make them less reliable.

For the southernmost part of the subduction zone the bounce points sample near but not on top of the slab contour and produce slightly deeper estimates of 410 depths. Cluster SA4 produces clean stacks with estimates of 413 and 415 km for both *sS* and *sP* and 412 km for *pP*. For the last cluster SA5 both the *sP* and *pP* stacks have low errors but give estimates which differ by 8 km: 409 and 401 km, respectively. However, comparing these results to cluster SA4 shows an elevation of about 7 km which is consistent between the two different phases.

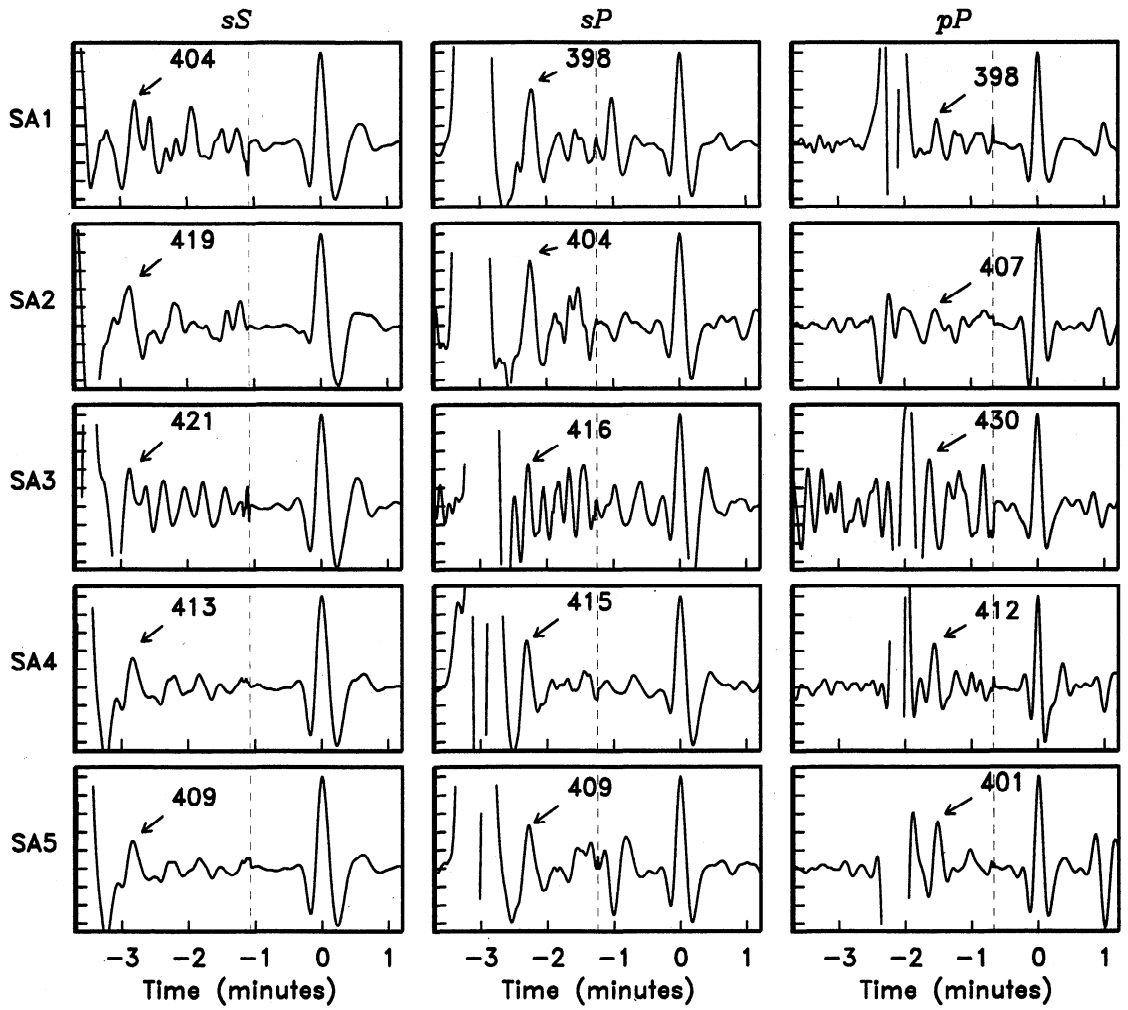

Figure 12. LP_{SRO} *sS*, *sP*, and LP *pP* stacks for five different locations in South America. The trace to the left of the dashed line is magnified by a factor of 10 for display purposes. Where a clear 410 peak is identified, the corresponding depth is labeled with an arrow and is listed in Table 2 along with its standard error. These stacks indicate lateral variations in the depth to the 410 of about 15 km with the discontinuity shallowest toward the north.

Table 2. Raw 410 Depth Estimates for South America Subduction Zone

Region	*sS*			*sP*			*pP*		
	Number of Data	Depth, km	±σ, km	Number of Data	Depth, km	±σ, km	Number of Data	Depth, km	±σ,* km
SA1	34	404	3	53	398	3	31	398	3
SA2	29	419	3	47	404	2	19	407	8
SA3	7	421	12	6	416	8	6	430	9
SA4	121	413	2	59	415	2	49	412	3
SA5	107	409	3	92	409	2	20	401	2

* Uncertainties are one standard deviation computed from bootstrap algorithm.

Depth estimates from the southern clusters are greater overall and in closer agreement with the regional depth estimate provided by the *SS* precursors (414 km), while for the northern bounce points the local depth estimates (398 to 404 km) are significantly shallower than the *SS* precursor estimate. This could be evidence for a localized shallowing of the 410-km discontinuity of 10 to 18 km in this region, suggesting the presence of a cold thermal anomaly behind the slab as the bounce points do not appear to sample the slab directly. Alternatively, the location of the slab plotted in Figure 11 could have a significant uncertainty because it is produced by fitting a curve to a pattern of seismicity, but there is a pronounced lack of earthquakes between 300 and 500 km depth in South America.

7. Tonga Subduction Zone

Sufficient data are available from the Tonga subduction zone that more detailed mapping of the 410-km discontinuity is possible. This is motivated not only by the extensive data coverage but by the muted and broad appearance of the *sS* stack for Tonga seen in Figure 8, indicating there may be complex structure to the 410 in this region. Figure 13 illustrates our 410 bounce point locations relative to the 400-km slab contours as determined by *Billington* [1980] and *Gudmundsson and Sambridge* [1998], both produced by fitting surfaces to patterns of seismicity and varying depths. Note that these studies plot the 400-km contour in slightly different places; the 50 to 100 km offsets provide us with a rough estimate of the uncertainty in the slab position. However, the Gudmundsson and Sambridge contour may be more accurate as it was derived using the more recent relocated earthquake catalog of E. R. Engdahl et al. (manuscript in preparation, 1997).

The *sS*, *pP*, and *sP* bounce points sometimes fall into natural clusters, for example, T8, but often do not, and there is no single best way to divide the data. There is a trade-off between including large numbers of records for stability in the stack (at the cost of lateral resolution) and dividing into many different groups to increase the resolution (at the cost of increasing the noise in the stacks due to the smaller number of data). We experimented with a variety of different clustering schemes including stacking data at different subhorizontal distances away from the slab in elongated regions roughly parallel to the 400 km depth contour (as shown in Figure 13) in order to search for topographic variations perpendicular to the slab. However, this resulted in many stacks with broad or multiple precursor peaks indicating more complicated structure on the 410 than is generally assumed. After examining several combinations, we finally identify the eight groups plotted in Figure 13 as providing the clearest 410-km peaks for a reasonable number of records in the stacks. The size of these groups is also comparable to the Fresnel zones of the depth phases.

The average regional 410 depth for Tonga from the *SS* precursor stack is 431 km (Figure 8). A finer division of the data is not possible for the *SS* precursors due both to the much poorer lateral resolution of the *SS* precursors and to the limited number of *SS* bounce points near Tonga. For most of the Tonga subgroups the *sS* and *sP* depth estimates generally agree fairly well; the *pP* depth estimates are often significantly shallower, though they show a roughly similar trend to the *sS* and *sP* results. As discussed in section 4, the source for this discrepancy may be in the velocity model used to compute the depths.

Cluster T1 is located at the northern end of the Tonga bounce points, about 200 km west of the slab intersection point. The *sS* and *sP* depth estimates are 423 and 432 km, respectively (see Figure 14 and Table 3), in good agreement with the regional *SS* estimate, while the *pP* stack gives 411 km. Cluster T2 is located closer to the slab intersection, but the 410 depth estimates from *sP* (426 km) and *sS* (401 km) are conflicting; the *sP* stack has a better defined peak. The *pP* result for this cluster, with an estimate of 397 km, indicates a 20 km elevation of the 410. Moving southward, cluster T3 suggests slightly shallower 410 depths from the *sS* and *pP* stacks (427 to 425 km) with a 12 km change in depth closer to the slab intersection point as measured from the *sS* stack in cluster T4. Alternatively, the *pP* stacks indicate a roughly flat depth to the discontinuity with estimates of 413 km (T3) to 406 km (T4), but the T4 cluster has a large standard error. Thus, in the northern part of Tonga, there appear to be slightly greater changes in 410 depths in a direction parallel to the slab than in a direction perpendicular to the slab.

Cluster T5, just to the south of T4 and located near the slab intersection point, yields a *sS* depth estimate of 394 km which indicates a substantial shallowing of the 410, in contrast to cluster T6 which yields 423 km. Similarly, the *sP* stacks indicate a shallowing near the slab but of lesser amplitude with estimates of 409 and 421 km for T5 and T6, respectively. The *pP* stacks also yield a 10 km shallower depth near the slab, but both the T5 and T6 stacks for *pP* have larger standard errors (see Table 3). Farther south, cluster T7 yields divergent *sS* and *sP* depth estimates of 401 and 415 km. Finally, the isolated cluster T8 results in depth estimates of 427 and 430 km (for *sS* and *sP*), again in good agreement with the regional *SS* precursor 410 depth of 431 km.

Overall, the variation in depth to the 410 along the strike of the slab is about 8 to 20 km, while the variation perpendicular to the slab is somewhat larger at about 32 to 40

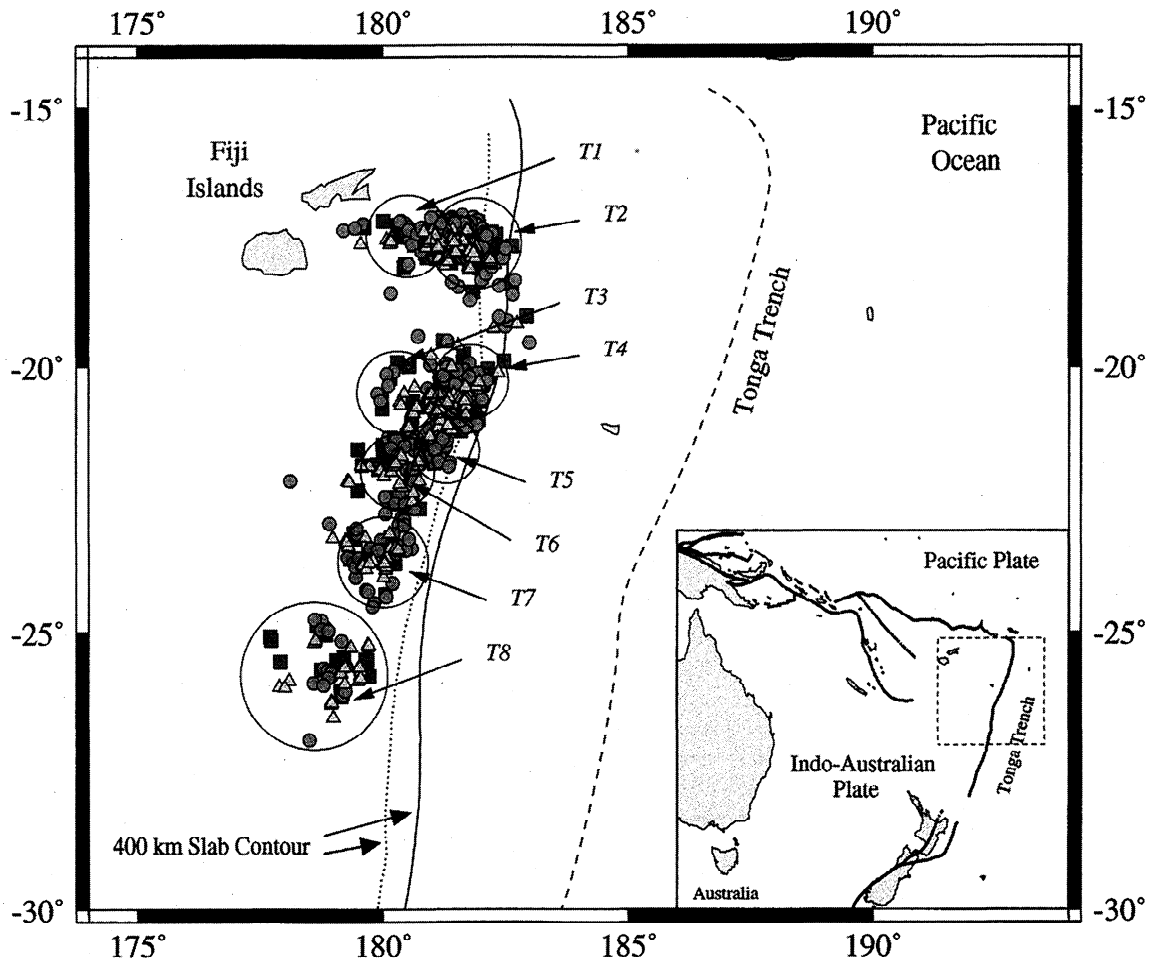

Figure 13. Mercator projection of the Tonga subduction zone together with the bounce points of *s*410*S* (circles), *s*410*P* (triangles), and *p*410*P* (squares) as they sample 400 km depth. Contours of the Tonga slab are shown at the surface trench (long-dashed line) and at 400 km depth as taken from two studies: after *Billington* [1980] (short-dashed line) and after *Gudmundsson and Sambridge* [1998] (solid line). Clusters of bounce points for which we obtain estimates of the 410 discontinuity are circled with labels corresponding to the depths listed Table 3. The circles show only the approximate locations of the different clusters; there is no sharing of data between subgroups in the actual data stacks.

km. However, the depth estimates do not always agree between the different *sS, sP,* and *pP* phases. Some of this can be attributed to the standard errors in the measurements; in other cases (e.g., cluster T7) the differences appear too large to be due to random error. These discrepancies may reflect differences in the ray paths and Fresnel zones of the different phases, coupled with rapid lateral variations in structure. If so, unraveling the exact details of the 410 topography will be a difficult task. In any case, our results suggest that 410 depths inferred from a single ray geometry and bounce point grouping may not be reliable.

8. Corrections for Velocity Heterogeneity

As in any other study based on near-vertical reflection data, the relationship between time and depth must be determined from a reference velocity structure; hence the discontinuity locations derived from the procedures described above are only apparent depths relative to the velocity model used (oceanic PREM). We have chosen to ignore the biasing effect of large-scale three-dimensional velocity variations in the upper mantle by concentrating on differences between local depth estimates and regional depths inferred from *SS* precursors (computed from the same velocity model). However, slabs are thermally and chemically distinct from the surrounding mantle and seismic waves traveling through the slab incur significant amplitude and travel time anomalies. Therefore we need to address how strong local velocity anomalies associated with the descending Tonga slab might affect our observations of depth variations on the 410 discontinuity.

Regions of high and low velocity between surface and 400 km depth will introduce systematic errors in the differential times as measured between the *sS* and *s*410*S* phases and, consequently, the computed 410 depth estimates. For example, a slower upper mantle velocity (with respect to the reference velocity model) biases the discontinuity depth estimates to larger values by increasing the differential time. Conversely, faster upper mantle velocities will decrease the differential time and result in shallower depth estimates for the discontinuity. We make corrections for the possibility of rays traveling up a (fast) slab or through a (slow) backarc by using regional velocity models for both *P* and *S* waves which report

Table 3. Raw 410 Depth Estimates for the Tonga Subduction Zone

Region	*sS*			*sP*			*pP*		
	Number of Data	Depth, km	±σ, km	Number of Data	Depth, km	±σ, km	Number of Data	Depth, km	±σ,* km
T1	74	423	7	72	432	3	25	411	3
T2	42	401	3	157	426	2	72	397	5
T3	35	427	5	29	425	5	33	413	5
T4	41	413	4	87	405	5	63	406	11
T5	19	394	5	46	409	6	10	405	4
T6	23	423	6	30	421	2	35	414	9
T7	30	401	3	39	415	5	26	-	-
T8	60	427	3	61	430	2	85	416	8

* Uncertainties are one standard deviation computed from bootstrap algorithm.

velocity anomalies of 4-6% fast for the Tonga slab at intermediate depths and up to 4% slow in the upper 170 km of the Lau backarc basin [*van der Hilst*, 1995; *Zhao et al.*, 1996; *Xu and Wiens*, 1997].

We examine the Tonga groups (Figure 13) and identify those for which the ray paths might travel through the slab or backarc, calculate the travel time anomaly, and compute corrected depth estimates for the 410. Groups T1, T3, and T8 largely comprise rays traveling to the north and west through regions of relatively homogeneous upper mantle beneath the South Fiji Basin, Fiji Plateau, and Lau Ridge, and therefore we do not apply corrections to these stacks. Groups T2, T4, and T5 clearly have rays traveling near or in the slab, while T6 and T7 mostly contain rays traveling both near and away from the slab. Furthermore, the groups containing upgoing rays near the slab are also the ones traveling through the slow backarc region in which case the corrections may at least partially cancel each other out. Also problematic is the fact that most clusters have rays which travel at widely different azimuths making it difficult to apply a single correction for each cluster.

In most cases, we estimate that the rays travel up the slab for less than 100 km and accrue rather small travel time anomalies: 1.2 s for *sS*, 0.9 s for *sP*, and 0.5 s for *pP* which translate to 2.8, 3.0, and 2.5 km, respectively. For the backarc the anomalies are slightly larger and opposite in sign: -1.8 s for *sS*, -1.1 s for *sP*, and -0.7 s for *pP*, which translate to -4.3, -3.6, and -3.4 km respectively. In some cases these depth corrections are roughly the same order of magnitude as the standard errors listed in Table 3. These factors preclude us from applying specific corrections to each cluster shown in Figure 13, as they may not be physically reasonable. Instead, we present here a perhaps crude but conservative set of corrections for the maximum amplitude of the 410 topography.

On the basis of the corrections computed above, the shallowest estimates for the 410 depth may be too shallow by up to about 3 km; conversely, the deepest estimates will be ~4 km too deep. Thus the cross-strike variation discussed above, with a maximum of 32 to 40 km would be reduced to 25 to 33 km peak-to-peak, while the along strike variation would be reduced from 20 km maximum to 13 km. The ability to resolve lateral variations to the depth of the 410 reflector within a single data set is a major advantage of this technique, and the observation of ~30 km of topography over horizontal scale lengths of only 200 to 300 km remains a robust one.

Variations in crustal thickness and velocity may also affect the calculation of the depth estimates but appear to be a less significant factor than the mantle heterogeneity since most rays are bouncing in oceanic crust which has little effect on the LP_{SRO} waveforms. The LP waveforms may be more susceptible to distortion due to crustal interaction, but such effects are seen to be averaged out in the stacks. Therefore we do not make corrections for any possible travel time anomalies associated with variable crustal structures.

9. Comparisons With Other 410 Studies

A number of previous studies were important for establishing the existence and observability of the underside 410-km reflections in subduction zones. *Vidale and Benz* [1992] (hereinafter referred to asVB92) used a large, short-period array with 881 stations in the western United States to stack *pP* arrivals from seven deep earthquakes in a number of subduction zones. They identified *p*410*P* phases from Tonga, South America, and the Marianas and inferred 410 depths ranging from 387 to 408 km. It is misleading to compare these results directly with our study because the VB92 depths were computed using a different velocity model (iasp91), and the resolution of their short-period data is higher than the longer-period data that we analyze here. We estimate that the use of the iasp91 model will produce 410 depth estimates that are systematically shallower (by 12 km for *sS*, 13 km for *sP*, and 16 km for *pP*) than those obtained using oceanic PREM, at 25 s period, due largely to the thicker crust in iasp91. Similarly, using standard PREM will produce 410 depths that are systematically shallower (by 16 km for *sS*, 14 km for *sP*, and 12 km for *pP*) than those obtained using oceanic PREM, both at 25 s period. The VB92 depths adjusted to oceanic PREM are 420 km for the Marianas and 399 to 410 km for Tonga; to compare with our South America result, the VB92 depth estimate is 410 km after adjusting to standard PREM. These values are in reasonable agreement with our *sS* and *sP* results for both the Marianas and the southernmost part of South America (see Figure 12) as the VB92 event falls in cluster SA5. In Tonga the VB92 events fall in clusters T5 and T7 and the estimates of 399 (for T5) and 410 (T7) roughly agree with our results for Tonga in that they show a similar offset of about 10 km. We note that the apparent elevation of the 410-km discontinuity near slabs discussed by VB92 may be largely a result of their use of the iasp91 model to infer discontinuity depths.

Zhang and Lay [1993] stacked long-period *SH* waves recorded by World-Wide Standardized Seismographic Network (WWSSN) instruments and identified *s*410*S* arrivals in events from the Japan and Kuril subduction zones, obtaining 410

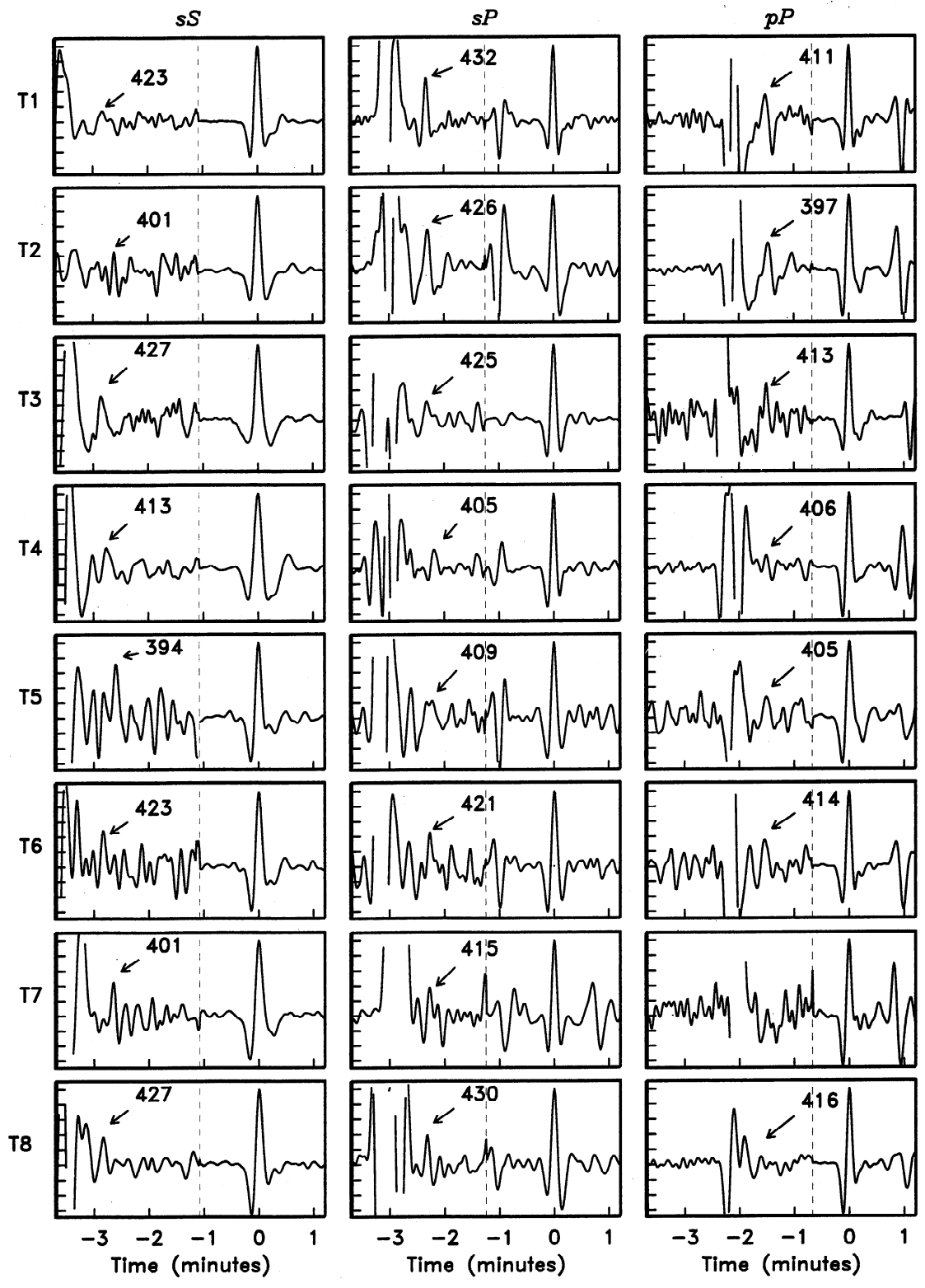

Figure 14. LP *sS*, *sP*, and *pP* stacks for eight different locations in the Tonga subduction zone. The trace to the left of the dashed line is magnified by a factor of 10 for display purposes; uncertainty bounds are not shown for clarity. These stacks indicate significant topography on the 410 discontinuity over very short length scales both perpendicular to and along strike of the slab. Lateral variations in the depth to the 410 are about 20 km along the strike of the slab and up to 40 km perpendicular to the slab.

depth estimates between 380 and 400 km. In a study of short-period and broadband *pP* and *sP* waveform stacks from four South American events (one in cluster SA2 and three within the clusters SA4 and SA5), *Ritsema et al.* [1995] observed consistent 410 reflections and inferred a discontinuity depth of 405 km using iasp91 as a reference velocity model. This estimate would be 409 km using standard PREM, so their observed depth agrees reasonably well with the values of 404 km for group SA2 and 415 to 409 km that we obtain for the SA4 and SA5 clusters from the *sP* stacks (Figure 12). An examination of *ScS* reverberations sampling South America by *Clarke et al.* [1995] revealed a slightly elevated estimates of 395 to 410±3 km for the discontinuity beneath Bolivia (near group SA2 in Figure 11). They interpret this shallowing to indicate colder temperatures in the mantle adjacent to the slab which is consistent with our observations of a shallower 410 in the northern part of the Peru-Chile subduction zone.

Recently, *Collier and Helffrich* [1997] stacked short-period *P* wave data from the U.K. and northwestern U.S. networks for 21 earthquakes of depth 40 to 550 km in the Izu-Bonin subduction zone and identified both topside *S*410*P* converted phases and underside *s*410*P* and *p*410*P* reflected phases. They map lateral variations in 410 depth that appear correlated with the slab geometry and infer an elevation of the 410 of up to 60 km within the core of the subducting slab. They also used iasp91 as a reference velocity model; the use of oceanic PREM would reduce their elevation to 44 km, still larger than any we observe in this study. However, we are unable to obtain any results for Izu-Bonin due to a lack of seismicity deeper than 550 km; thus we can not make direct comparisons with the *Collier and Helffrich* [1997] study.

10. Discussion

There exists some difficulty in reconciling the observed seismic structure of the 410-km discontinuity with laboratory and thermodynamic models of the prevailing $\alpha-$ to $\beta-$ olivine phase transition. Recent work focusing on the sharpness of the discontinuity [*Vidale et al.*, 1995; *Benz and Vidale,* 1993; *Helffrich and Wood*, 1996; *Neele,* 1996; *Melbourne and Helmberger*, 1998] has shown that the 410 interface must be quite sharp, at least in some locations, with a significant velocity jump occurring in less than about 5 km. This is substantially less than the total depth interval over which the phase change is expected to occur. Various mechanisms have been proposed to reconcile this conflict, including a non-equilibrium phase transition [*Solomatov and Stevenson*, 1994], accompanying transformation of a garnet-pyroxene component [*Anderson*, 1989], hydration effects [*Wood*, 1995], and the possible coincidence of the olivine phase change with a sharp contrast in composition or degree of partial melt [*Nolet and Zielhuis*, 1994; *Revenaugh and Sipkin,* 1994]. Other authors have emphasized that the velocity increase across a phase transition is not expected to be linear, as has commonly been assumed in interpretation of the seismic results and that a substantial fraction of the total velocity increase occurs over a relatively short depth interval [e.g., *Bina* and *Helffrich,* 1994; *Stixrude*, 1997].

Another possible discrepancy between seismic observations and mineral physics predictions concerns the amplitude of topography on the 410-km discontinuity. Maps of large-scale 410 topography [e.g., *Shearer*, 1993; *Flanagan and Shearer,* 1998] indicate variations of 20 to 25 km,

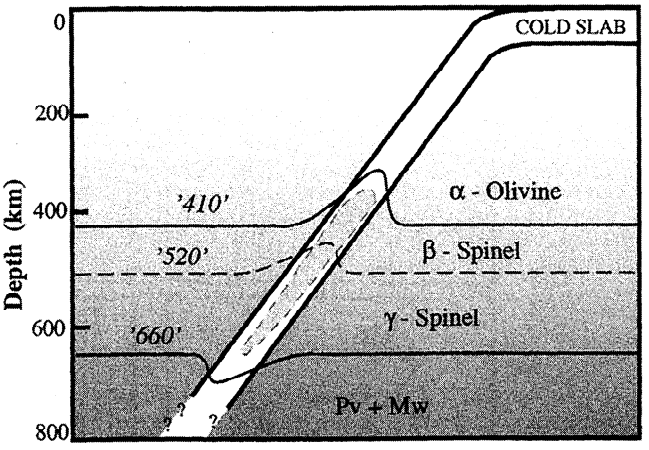

Figure 15. Schematic cross section of a subduction zone illustrating two possible configurations of topography on the 410-km velocity discontinuity. In the equilibrium $\alpha-$ to $\beta-$ phase transition case, the boundary would be deflected upward in the cold interior of the slab; conversely, in the kinetically inhibited case, the boundary is quite narrow and deflected downward (the metastable α-olivine wedge in the shaded region).

significantly less than the observed 660 topography. *Bina and Helffrich* [1994] argue that the expected 410 Clapeyron slope is steeper than that at 660 such that 410 topography should be greater than 660 topography, and they suggested that larger topographic variations on the 410 might be masked in some way from seismic observations. Recently, *Dueker and Sheehan* [1997] examined *P*-to-*S* converted phases in the western United States and found evidence for 20 to 30 km of transition zone thickness variations over lateral scale lengths as short as 200 to 300 km. If temperature alone is controlling the discontinuity depths (i.e., through the Clapeyron slopes), this would require vary large lateral temperature gradients in the transition zone.

Subducting slabs can affect the topography on the 410-km discontinuity in two different ways (illustrated in Figure 15). First, there is the direct thermal effect of the cold slab on the 410-km phase change. This should induce elevated 410 topography within the slab and in the surrounding mantle to the extent that the adjacent mantle material is cooled by the descending slab. Assuming a Clapeyron slope of 2.9 MPa/°K [*Bina and Helffrich*, 1994], a 100° change in temperature will produce an approximate 8 km change in 410 topography. Thermal anomalies of 600° to 1000° are obtained for the center of slabs at 400 km depth from finite difference modeling (results vary depending upon the age and thickness of the slab and the subduction rate), predicting 50 to 80 km in elevation on the 410-km discontinuity, but the maximum anomalies are confined to a narrow region less than 50 km across. The 410 elevation will be reduced toward the edges of the slabs, and the entire anomalous thermal region is only 100 to 150 km in lateral width (shallow dipping slabs predict a wider elevated region on the 410).

Second, there is the possible kinetic depression of the 410-km discontinuity that may cause a metastable wedge of olivine to exist well below 410 km, a scenario that has been proposed as a possible mechanism for the origin of deep earthquakes (see review by *Kirby et al.*, [1996]). This wedge may extend to the depth of the deepest earthquakes in the subduction zone.

The resulting 410 topography could be quite severe, but the anomalous region may only be 50 to 100 km across at 400 km depth.

Can our results be used to confirm any of these predictions? To first order, our 410 depth estimates generally do not show a large difference between local near-slab depths and regional estimates derived from *SS* precursors. For most of our data the 410 precursor bounce points are 100 to 300 km away from the slab, and these results are consistent with a narrow thermal anomaly confined to the slab and not extending very far into the surrounding mantle. Two exceptions are the northern part of the South American data, where an elevation of the 410 is observed about 100 km east of the slab, and group T7 in Tonga, ~100 km the west of the slab. These elevations suggest a cold thermal anomaly at some distance from the slab and could indicate a broad thermal halo produced from the slab cooling the adjacent mantle more effectively in certain locations [*Vidale and Benz*, 1992; *Collier and Helffrich*, 1997].

In a few cases (Marianas, several of the Tonga caps) the bounce points appear to sample the 410-km discontinuity within the subducting slab itself. A possible slight depression (10 km) is observed for the Marianas; one of the Tonga caps (T5) suggests a large elevation (up to 40 km) of the 410, but the other near-slab caps (T2 and T4) indicate only 0 to 15 km of elevation. Tonga is the location of the most rapidly subducting (Pacific) plate and thus is the most likely place to observe the metastable wedge of olivine. However, the along-strike variations in 410 depths observed in Tonga are hard to explain with a simple thermal model of a subducting slab, and the shape of the Tonga slab as imaged from seismicity is far from simple [*Billington*, 1980; *Gudmundsson and Sambridge*, 1998].

Unfortunately, the lateral resolution of the depth phase precursors is probably not sufficient to resolve narrow 410 anomalies within the central core of the descending slabs. The $s410S$, $s410P$, and $p410P$ Fresnel zones vary in width, depending upon the phase, the earthquake depth and the frequency content of the data but are generally about 200 km across. It is not clear the extent to which these data will be affected by steep but narrow (50 to 100 km wide) ridges or troughs in the 410-km discontinuity; as seen in Figure 15, the topography can have quite an irregular shape. Kirchhoff or other synthetic seismogram modeling may help resolve this issue but is beyond the scope of this paper.

Regarding the discrepancy between the *pP* and *sS* precursor estimates for the 410, the *P* waves inherently have higher frequency content and thus should reflect off the sharpest part of the discontinuity. Current mineralogical [*Helffrich and Wood*, 1996; *Stixrude*, 1997] and seismological [*Melbourne and Helmberger*, 1998] models indicate a frequency dependent discontinuity for the 410. *Stixrude* [1997] states that the phase transition can be modeled as a layer in which the velocity increases nonlinearly, most of the increase occurring in only one-third of the transition depth interval. Therefore, at longer periods the discontinuity might appear at different depths than at shorter periods, which are more sensitive to the sharpest portion of the velocity jump. However, we are not able to resolve a significant frequency dependence (within the range 0.01 to 0.12 Hz) in the apparent depths obtained from a single phase geometry (e.g., Figure 7). The possible difference between the *P*-to-*S* velocity ratio in the subduction zones examined and that given by PREM remains the best explanation for the discrepancy of 410 depths computed from the *sS* and *pP* phases.

Acknowledgments. This work has benefited from discussions with T. Lay and J. Vidale. We thank M. Sambridge for providing the slab contours in Figures 9, 10 , 11, and 13 prior to publication; P. Wessel and W. Smith are acknowledged for developing the GMT software used to generate the maps. We are grateful to H. Bolton, G. Masters, and J. Um for their help in maintaining the large, long-period database at IGPP and to the IRIS, IDA, and Geoscope networks for supplying the data. We thank G. Anderson, L. Astiz, and R. van der Hilst for providing many helpful comments on the manuscript and Y. Gu and G. Bock for their detailed reviews. This research was supported by NSF grant EAR96-14350. M.P.F. is supported by a U.C. President's Postdoctoral Fellowship, NSF Postdoctoral Fellowship, and the Cecil H. and Ida M. Green Foundation.

References

Anderson, D. L., *Theory of the Earth*, 366 pp., Blackwell Sci., Cambridge, Mass.,1989.

Benz, H. M., and J. E. Vidale, Sharpness of upper-mantle discontinuities determined from high-frequency reflections, *Nature, 365*, 147-150, 1993.

Billington, S., The morphology and tectonics of the subducted lithosphere in the Tonga-Fiji-Kermadec region from seismicity and focal mechanism solutions, Ph. D. thesis, 220 pp., Cornell Univ., Ithaca, N.Y., 1980.

Bina, C. R., and G. Helffrich, Phase transition Clapeyron slopes and transition zone seismic discontinuity topography, *J. Geophys. Res., 99*, 15,853-15,860, 1994.

Bina, C. R., and B. J. Wood, Olivine-spinel transitions: Experimental and thermodynamic constraints and implication for the nature of the 400-km seismic discontinuity, *J. Geophys. Res., 92*, 4853-4866, 1987.

Bock, G., and R. Kind, A global study of *S*-to-*P* and *P*-to-*S* conversions from the upper mantle transition zone, *Geophys. J. Int., 107*, 117-129, 1991.

Castle, J. C., and K. C. Creager, Seismic evidence against a mantle chemical discontinuity near 660 km depth beneath Izu-Bonin, *Geophys. Res. Lett., 24*, 241-244, 1997.

Clarke, T. J., P. G. Silver, Y.-L. Yeh, D. E. James, T. C. Wallace, and S. L. Beck, Close in *ScS* and *sScS* reverberations from the 9 June 1994 Bolivan earthquake, *Geophys. Res. Lett., 22*, 2313-2316, 1995.

Collier, J. D., and G. Helffrich, Topography of the "410" and "660" km seismic discontinuities in the Izu-Bonin subduction zone, *Geophys. Res. Lett., 24*, 1535-1538, 1997.

Dueker, K. G., and A. F. Sheehan, Mantle discontinuity structure from midpoint stacks of converted *P* to *S* waves across the Yellowstone hotspot track, *J. Geophys. Res., 102*, 8313-8327, 1997.

Dziewonski, A. M., and D. L. Anderson, Preliminary reference Earth model, *Phys. Earth Planet. Inter, 25*, 297-356, 1981.

Flanagan, M. P., and P. M. Shearer, Global mapping of topography on transition zone velocity discontinuities by stacking *SS* precursors, *J. Geophys. Res., 103*, 2673-2692 1998.

Gossler, J., and R. Kind, Seismic evidence for very deep roots of continents, *Earth Planet. Sci. Lett., 138*, 1-13, 1996.

Gu, Y., and A. M. Dziewonski, Global topography of upper mantle discontinuities from *SS* precursors, *Eos Trans AGU, 77(46)*, Fall Meet. Suppl., F472, 1996.

Gudmundsson, O., and M. Sambridge, A regionalized upper mantle (RUM) seismic model, *J. Geophys. Res., 103*, 7121-7136, 1998.

Helffrich, G., and J. Brodholt, Relationship of deep seismicity to the thermal structure of subducted lithosphere, *Nature, 353*, 252-255, 1991.

Helffrich, G., and B. Wood, 410-km discontinuity sharpness and the form of the olivine α-β phase diagram: Resolution of apparent seismic contradictions, *Geophys. J. Int., 126*, F7-F12, 1996.

Helffrich, G. R., S. Stein, and B. J. Wood, Subduction zone thermal structure and mineralogy and their relationship to seismic wave reflections and conversions at the slab/mantle interface, *J. Geophys. Res., 94*, 753-763, 1989.

Iidaka, T., and Y. Furukawa, Double seismic zone for deep earthquakes in the Izu-Bonin subduction zone, *Science, 263*, 1116-1118, 1994.

Iidaka, T., and D. Suetsugu, Seismological evidence for metastable olivine inside a subducting slab, *Nature, 356*, 593-595, 1992.

Inoue, T., H. Yurimoto, and Y. Kudoh, Hydrous modified spinel,

$Mg_{1.75}SiOH_{0.5}O_4$: A new water reservoir in the mantle in the mantle transition region, *Geophys. Res. Lett., 22*, 117-120, 1995.

Katsura, T., and E. Ito, The system Mg_2SiO_4-Fe_2SiO_4 at high pressures and temperatures: Precise determination of stabilities of olivine, modified spinel, and spinel, *J. Geophys. Res., 94*, 15,663-15,670, 1989.

Kennett, B. L. N., *IASPEI 1991 Seismological Tables*, 167 pp., Res. Sch. of Earth Sci., Aust. Natl. Univ., Canberra, 1991.

King, S. D., and B. H. Hager, Subducted slabs and the geoid, 1, Numerical experiments with temperature-dependent viscosity, *J. Geophys. Res., 99*, 19,843-19,852, 1994.

Kirby, S. H., Localized polymorphic phase transformations in high-pressure faults and applications to the physical mechanism of deep earthquakes, *J. Geophys. Res., 92*, 13,789-13,800, 1987.

Kirby, S. H., S. Stein, E. A. Okal, and D. C. Rubie, Metastable mantle phase transformations and deep earthquakes in subducting oceanic lithosphere, *Rev. Geophys., 34*, 261-306, 1996.

Melbourne, T., and D. Helmberger, Fine structure of the 410-km discontinuity, *J. Geophys. Res., 103*, 10,091-10,102, 1998.

Molnar, P., D. Freedan, and J. S. H. Shih, Lengths of intermediate and deep seismic zones and temperatures in downgoing slab of lithosphere, *Geophys. J. R. Astron. Soc., 56*, 41-54, 1979.

Myers, S. C., T. C. Wallace, S. L. Beck, P. G. Silver, G. Zandt, J. Vandecar, and E. Minaya, Implications of spatial and temporal development of the aftershock sequence for the M_W 8.3 June 9, 1994 deep Bolivian earthquake, *Geophys. Res. Lett., 22*, 2269-2272, 1995.

Neele, F., Sharp 410-km discontinuity from short-period *P* reflections, *Geophys. Res. Lett., 23*, 419-422, 1996.

Nolet, G., and A. Zielhuis, Low *S* velocities under Tornquist-Teisseyre zone: Evidence for water injection into the transition zone by subduction, *J. Geophys. Res., 99*, 15,813-15,820, 1994.

Revenaugh, J. S., and T. H. Jordan, A study of mantle layering beneath the western Pacific, *J. Geophys. Res., 94*, 5787-5813, 1989.

Revenaugh, J. S., and T. H. Jordan, Mantle layering from *ScS* reverberations, 3, The upper mantle, *J. Geophys. Res., 96*, 19,781-19,810, 1991.

Revenaugh, J. S., and S. A. Sipkin, Seismic evidence for a silicate melt atop the 410-km mantle discontinuity, *Nature, 369*, 474-476, 1994.

Richards, M. A., and C. W. Wicks, *S-P* conversion from the transition zone beneath Tonga and the nature of the 670 km discontinuity, *Geophys. J. Int., 101*, 1-35, 1990.

Ringwood, A. E., *Composition and Petrology of the Earth's Mantle*, 618 pp., McGraw-Hill, New York, 1975.

Ritsema, J., M. Hagerty, and T. Lay, Comparison of broadband and short-period seismic waveform stacks: Implications for upper-mantle discontinuity structure, *Geophys. Res. Lett., 22*, 3151-3154, 1995.

Schubert, G., D. A. Yuen, and D. L. Turcotte, Role of phase transitions in a dynamic mantle, *Geophys. J. R. Astron. Soc., 42*, 705-735, 1975.

Shearer, P. M., Seismic imaging of upper-mantle structure with new evidence for a 520-km discontinuity, *Nature, 344*, 121-126, 1990.

Shearer, P. M., Constraints on upper mantle discontinuities from observations of long-period reflected and converted phases, *J. Geophys. Res., 96*, 18,147-18,182, 1991.

Shearer, P. M., Global mapping of upper mantle reflectors from long-period *SS* precursors, *Geophys. J. Int., 115*, 878-904, 1993.

Shearer, P. M., Transition zone velocity gradients and the 520-km discontinuity, *J. Geophys. Res., 101*, 3053-3066, 1996.

Silver, P. G., S. L. Beck, T. C. Wallace, C. Meade, S. C. Myers, D. E. James, and R. Kuehnel, Rupture characteristics of the deep Bolivian earthquake of 9 June 1994 and the mechanism of deep-focus earthquakes, *Science, 268*, 69-73, 1995.

Solomatov, V. S., and D. J. Stevenson, Can sharp seismic discontinuities be caused by non-equilibrium phase transformations?, *Earth Planet. Sci. Lett., 125*, 267-279, 1994.

Stixrude, L., Structure and sharpness of phase transitions mantle discontinuities, *J. Geophys. Res., 102*, 14,835-14,852, 1997.

van der Hilst, R., Complex morphology of subducted lithosphere in the mantle beneath the Tonga trench, *Nature, 374*, 154-157, 1995.

van der Hilst, R., R. Engdahl, W. Spakman, and G. Nolet, Tomographic imaging of subducted lithosphere below northwest Pacific island arcs, *Nature, 353*, 37-42, 1991.

Vidale, J. E., and H. M. Benz, Upper-mantle seismic discontinuities and the thermal structure of subduction zones, *Nature, 356*, 678-683, 1992.

Vidale, J. E., X.-Y. Ding, and S. P. Grand, The 410-km depth discontinuity: A sharpness estimate from near-critical reflections, *Geophys. Res. Lett., 22*, 2557-2560, 1995.

Vinnik, L. P., Detection of waves converted from *P* to *SV* in the mantle, *Phys. Earth Planet. Inter., 15*, 39-45, 1977.

Wiens, D. A., J. J. McGuire, and P. J. Shore, Evidence for transformational faulting from a deep double seismic zone in Tonga, *Nature, 364*, 790-793, 1993.

Wood, B. J., The effect of water on the 410-kilometer seismic discontinuity, *Science, 268*, 74-76, 1995.

Xu, Y., and D. A. Wiens, Upper mantle structure of the southwest Pacific from regional waveform inversion, *J. Geophys. Res., 102*, 27,439-27,451, 1997.

Yamazaki, A., and K. Hirahara, The thickness of upper mantle discontinuities, as inferred from short-period J-array data, *Geophys. Res. Lett., 21*, 1811-1814, 1994.

Zhang, Z., and T. Lay, Investigation of upper mantle discontinuities near northwestern Pacific subduction zones using precursors to *sSH*, *J. Geophys. Res., 98*, 4389-4405, 1993.

Zhao, D., Y. Xu, D. Wiens, L. Dorman, J. Hildebrand, S. Webb, and W. Crawford, Depth extent of the Lau backarc spreading center and its relationship to the deep subduction process, *Eos Trans. AGU, 77(46)*, Fall Meet. Suppl.,F498, 1996.

M. P. Flanagan and P. M. Shearer, IGPP-0225, Scripps Institution of Oceanography, University of California at San Diego, 9500 Gilman Drive, La Jolla, CA 92093-0225. (e-mail: megan@mahi.ucsd.edu; shearer@mahi.ucsd.edu)

(Received August 14, 1997; revised January 28, 1998;
accepted February 4, 1998)